Synthesis and Characterization Cu^{+}:InP/$ZnSe_{1-x}S_x$ Quantum Dots

For Luminescent Solar Concentrator Applications

Date:	03-04-2018
Student:	Dirk Spruijt
Student number:	5774772
University:	Utrecht University
Master program:	Nanomaterial Science
Course:	Master thesis
Research group:	Condensed Matter and Interfaces
Daily supervisor:	P. T. Prins, MSc.
First examiner:	prof. dr. D.A.M. Vanmaekelbergh
Second examiner:	dr. C. De Mello Donega

Abstract

Solar energy has been an important topic of research as an alternative energy source for fossil fuels. However, the photovoltaic (PV) cells currently commercialized are unsuitable for transparent surfaces (e.g. windows). Luminescent solar concentrators (LSCs) offer a solution for this particular problem, however, the current LSCs have low efficiencies due to reabsorption of photons emitted by the luminescent materials within the LSC. In this paper, research is performed on Cu^+:InP/$ZnSe_{1-x}S_x$ quantum dots (QDs), a potential luminescent material for LSCs with reduced reabsorption. Cu^+:InP/$ZnSe_{1-x}S_x$ QDs are synthesized utilizing a hot-injection synthesis, followed by post-synthesis doping and shell growth. Variation in shell thickness and copper dopant concentration are performed as well. The resulting samples are characterized with absorption and emission spectroscopy, time resolved emission spectroscopy, inductive coupled plasma – optical emission spectroscopy, and transient absorption spectroscopy. A down-shifted emission (600 meV) and a longer lifetime (one order of magnitude) are observed for the Cu^+:doped system compared to the undoped system. Upon decreasing the Cu^+ concentration in the QDs, the luminescence and lifetime increase, while increasing the shell increases the luminescence.

Contents

1 Introduction 1
2 Theory 3
2.1 Luminescent Solar Concentrators 3
2.2 Quantum Dots 5
2.2.1 Doping 7
2.2.2 Traps and passivation 7
2.3 Formation of nanocrystals 11
2.3.1 Nucleation 11
2.3.2 Growth 12
2.3.3 Hot-injection and heat-up methods 13
2.4 Copper-doped Systems 15
2.5 Indium Phosphide 18
2.5.1 InP quantum dot synthesis 18
2.5.2 Size and concentration 19
2.5.3 Cu^+:InP quantum dots 20
2.6 Transient absorption spectroscopy 22
3 Materials and methods 23
3.1 Synthesis of Cu^+:InP/$ZnSe_{1-x}S_x$ QDs 23
3.2 Varying shell thickness 24
3.3 Varying copper concentration 24
3.4 Characterization 25
3.4.1 Absorption spectroscopy 25
3.4.2 Emission spectroscopy 25
3.4.3 ICP-OES 26
3.4.4 Transient absorption method 26
3.5 Chemicals 26
4 Results and discussion 27
4.1 Synthesis of the Cu^+:InP/$ZnSe_{1-x}S_x$ QDs 27
4.1.1 Synthesis of the InP cores 27
4.1.2 Doping and encapsulation in shell 29
4.2 Variation in the shell thickness 32
4.2.1 Encapsulated InP QDs 32
4.2.2 Encapsulated Cu^+:InP QDs 35
4.3 Variation in the copper dopant 38
4.3.1 ICP data 38

4.3.2 Absorption and emission data 39
4.3.3 Lifetime analyses 42
4.4 Transient absorption spectroscopy measurements 44
5 Conclusion 47
6 Outlook 49
7 Acknowledgements 51
8 References 53
Appendix 1: List of abbreviations and symbols 59
Appendix 2: Synthesis protocol 61
Appendix 3: Emission and QY measurements 63

1 Introduction

Climate change has always been an unescapable fact and has changed the earth over the course of its existence. Naturally, climate change is quite slow, occurring over centuries. Due to the large output of greenhouse gasses in modern society, the global warming is enhanced, leading to a warmer climate with several disadvantages such as extreme weather and rising sea levels. [1] CO_2 is a greenhouse gas, which is emitted in large amounts every day and is produced during the production of electrical energy by burning oil, coal, and other fossil fuels. [2] To inhibit the growth of enhanced global warning, CO_2 production must be decreased. Therefore, alternative sources of energy must be explored. [3] [4] These alternative energies should be sustainable and clean, which leaves wind, water, and solar energy. Solar energy production differs from the wind and water energy production methods, generally not relying on large power plants with turbines like most wind and water energy production methods, but it only requires small panels, which can be placed on top of houses. Two different kinds of energy can be harvested from the solar radiation: thermal and electrical energy. The latter is more interesting, because its more flexible in its usage.

A good policy to decrease the CO_2 emission is to construct buildings which provide their own power, utilizing alternative energy sources. [5] To avoid big energy plants, solar energy can be utilized, however, there are several problems with utilizing just photovoltaic (PV) cells. The first problem is the efficiency of the PV cell. Tall buildings in particular suffer from the efficiency of a commercial PV cell, which has maximum efficiency of 22.5%. [6] The roofs of these buildings do not supply enough surface area for PV cells to gather the necessary power needed to supply the entire building of energy. This would be solved by installing PV cells on other areas than the roof, resulting in the second problem that PV cells are not suitable for every location. The sides of buildings are often covered with windows, so the PV cells would have to be transparent. Transparent PV cells exist [7], but are expensive and less efficient. The third problem is that PV cells are expensive.

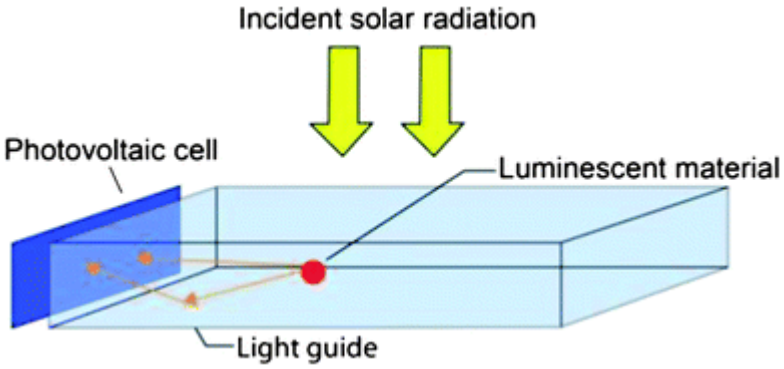

Figure 1: Luminescent solar concentrator. The incident light is captured in the light guide (waveguide) and down-shifted by luminescent material. Photovoltaic cells on the side converts the photons into electricity. Produced from [8].

LSCs may become a good solution for some of these problems. A LSC consists of a waveguide with luminescent material and concentrates solar radiation towards a PV cell on the sides, see Figure 1. The main reason for the start of the development of LSCs was to lower the costs of solar energy. [9] [10] [11] The LSC focusses the light of a large area on the relatively small PV cell on its sides, therefore, reducing the amount of expensive semiconductor material needed for the solar cells. Another advantage is that the LSCs can transparent and are capable of being incorporated into windows. Due to multiple loss mechanisms in LSCs, the current power conversion records stands at 7.1%. [12] These loss mechanisms can be divided into two categories, the radiative and the non-radiative losses. The waveguide causes most of the non-radiative losses, such as reflection, transparency, and escape cones. The luminescent material cause the radiative losses, such as quantum yield (QY) and

reabsorption. Due to the fact that LSCs will always have lower efficiencies than PV cells, they will never replace PV cells, but will likely be used in combination with PV cells. PV cells will still be used on top of the building, while LSCs will be incorporated into windows. Improvement of the current LSCs is needed before they will be of any real use.

Most of the losses are reducible by performing research on optimisation of the luminescent material in LSCs. Luminescent material based on QDs may be able to improve the current efficiency of LSCs. QDs are semiconductor nanocrystals with tuneable optical properties. These optical properties are tuneable for nanocrystals with sizes smaller than the exciton Bohr radius of the material, resulting confinement of electrons. Stronger confinement leads to a larger bandgap (E_g), consequently shifting absorption and emission towards the ultraviolet light. This tuneability allows selective absorption, which will aid in tailoring the luminescent material for more efficiency.

Reabsorption is one of the more severe contributors to the loss of efficiency and, therefore, reabsorption will have to be reduced. This reduction is possible utilizing heterostructured QDs or doped QDs. [13] [14] [15] [16] [17] [18] [19] These systems are able to down-shift the emission of the absorbed light, therefore, reducing the overlap between the absorption and re-emission and thus reducing re-absorption. The Type II heterostructured QDs down-shift the absorbed light by transferring an excited electron from the core conduction band (CB) to the shell CB. The CB of the shell has lower energy, therefore, emission will be redshifted. An example of such a system is CdTe/CdSe. [17] Certain doped QDs down-shift the absorbed light by placing energy levels inside the E_g of the QD. One or both of the charge carriers relax into these energy levels before recombination occurs, resulting in down-shifted emission. Examples of doped systems are Mn^{2+}:ZnSe [15] and Cu^{+}:CdSe [20], but also ternary QDs like $CuInS_2$ [20] and $CuInSe_2$ [21] (CIS and CISe, respectively).

This thesis focusses on the synthesis and characterization of Cu^{+}:InP/$ZnSe_{1-x}S_x$, which shows promise for LSCs due to several reasons. First, InP has the ability to absorb a large part of the solar spectrum, which increases the efficiency of the LSCs, because more light is converted and redirected towards the solar cell. Furthermore, Cu^{+}:InP down-shifts the emission separating the absorption and emission to reduce reabsorption, similar to Cu^{+}:CdSe and CIS. Another reason for research in this system, is because its properties are unknown, few paper have been published on this particular system. [20] [22] A $ZnSe_{1-x}S_x$ shell is grown around the Cu^{+}:InP in order to create a Type I heterostructured QD, increasing the QY of the system.

There are several goals during this research. The main goal is the synthesis and characterization of the Cu^{+}:InP/$ZnSe_{1-x}S_x$ QDs. Followed by optimization of the photo luminescent QY of this system by variation in shell growth. The final goal is to study the effect of the copper dopant concentration upon the optical properties of the Cu^{+}:InP/$ZnSe_{1-x}S_x$ QDs.

2 Theory

In this theory chapter, several topics are discussed, first is the general theory about LSCs and its loss mechanisms. Followed by a section on QDs in general, QD formation, copper-doped systems, and InP and Cu^+:InP. Lastly, there is background theory about transient absorption spectroscopy.

2.1 Luminescent Solar Concentrators

The LSCs are a possible method for the production of solar generated electricity in places where transparent surfaces are present (e.g. windows). [23] Figure 2 shows a simplified image of a LSC and its two components:

- Waveguide
- Luminescent material

The waveguide is made from a material with high refractive index (e.g. PMMA [24], refractive index 1.5), which causes total internal reflection, guiding the trapped light to the PV cell on the side of the LSC. [9] The luminescent material inside the LSC can hold multiple purposes. The foremost purpose of the luminescent material is to absorb light passing through the solar concentrator, before re-emitting it to the sides in order to trap the light within the waveguide. [9] Another important function of the luminescent material is the conversion of the absorbed light to higher wavelengths, causing UV radiation to be converted to visible light, which are converted better by most PV cells. The PV cell is a separate component, which converts the solar radiation into electric currents, and is placed on the side of the waveguide, where it will collect the photons for conversion.

The power conversion of 1 m^2 of LSC is not as efficient as 1 m^2 of PV cells, because the LSCs maximum power conversion is equal to that of the PV cell attached. Apart from the PV cell loss, LSCs suffer from other losses as well (Figure 2), therefore, LSCs are far from efficient at this moment. There are two types of losses in these LSCs:

- Non-emissive losses
- Emissive losses

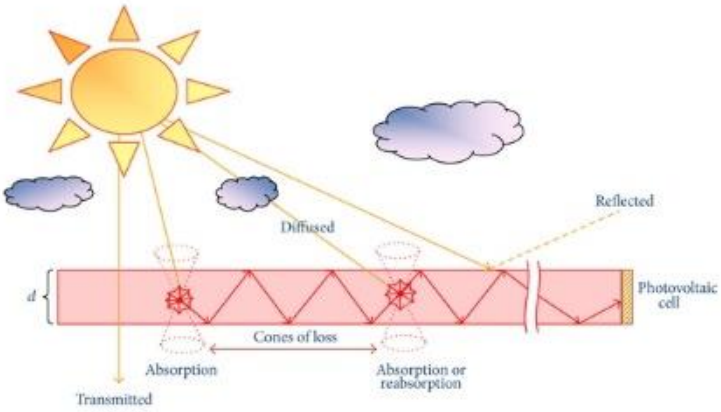

Figure 2: Luminescent solar concentrator with all the loss mechanisms. The three non-emissive losses are reflection, transmission, and the loss in power conversion by PV cell. The emissive losses consist of the QY, escape losses, and most important the reabsorption. Produced form [25].

There are three major non-emissive losses. The first non-emissive loss are the photons, which are not able to enter the LSC. These photons are reflected upon the surface of the LSC, the Fresnel loss. [9] The second non-emissive loss are the photons, which are transmitted through the LSC without being trapped inside the waveguide. This loss causes the transparent property, which one would desire in

case of the surface being a window. The final non-emissive loss is the efficiency of the power conversion by the PV cell.

There are three major emissive losses. The first of the emissive losses is the QY of the luminescent material. If the QY is 90% then a maximum of 90% of the re-emitted light can reach the PV cell. [9] The second emissive loss is the emission from a photon by luminescent material in the direction of the escape cones. [9] If a photon is emitted in the direction of the escape cones it will escape the LSC and therefore not reach the PV cell. The third and final emissive loss is reabsorption. [9] If a photon is emitted from a luminescent metal-organic complex or QD there is a large chance that it will be reabsorbed by another luminescent particle. This brings two problems loss due QY and loss due escape losses, the severity depending on the luminescent material concentration. Photons are likely to be absorbed several times before they will reach the PV cell.

The equations for the efficiency of the power conversion is constructed in equation 1, which shows that the total power conversion efficiency η_{tot} is the product of the optical efficiency of the LSC η_{opt} and the monochromatic efficiency of the PV cell η_{PV}^{*}. [26]

$$\eta_{\mathrm{Tot}} = \eta_{\mathrm{Opt}} \cdot \eta_{\mathrm{PV}}^{*} = (1 - R) \cdot \eta_{\mathrm{Abs}} \cdot \eta_{\mathrm{PL}} \cdot \eta_{\mathrm{Trap}} \cdot \eta_{\mathrm{RA}} \cdot \eta_{\mathrm{PV}}^{*} \tag{1}$$

In equation 1, η_{Opt} can expanded by inserting the efficiency losses mentioned above. *R* is the reflection of incident light off the waveguide, η_{Abs} is the absorption efficiency of the solar spectrum of the luminescent material, η_{Trap} is the trapping efficiency, η_{PL} is the efficiency of photoluminescence (QY) of the luminescent material, and η_{RA} is the efficiency of preventing reabsorption by the luminescent material. Each of these efficiencies can be calculated using the equations presented below. [26]

$$R = \frac{(n_{\mathrm{Sub}}-1)^2}{(n_{\mathrm{Sub}}+1)^2} \tag{2}$$

$$\eta_{\mathrm{Trap}} = \sqrt{1 - \frac{1}{n_{Sub}^2}} \tag{3}$$

$$\eta_{\mathrm{Abs}} = \frac{\int_{300\mathrm{nm}}^{E_{\mathrm{g}}^{\mathrm{Lum}}} \mathrm{AM1.5G}(\lambda)\cdot \mathrm{A}(\lambda)\cdot d(\lambda)}{\int_{300\mathrm{nm}}^{\infty} \mathrm{AM1.5G}(\lambda)\cdot d(\lambda)} \tag{4}$$

In which n_{Sub} is the refractive index of the LSC waveguide material, AM1.5G(λ) is the air mass 1.5 global solar flux spectrum, and A(λ) and $E_{\mathrm{g}}^{\mathrm{Lum}}$ are the absorption spectrum and the bandgap of the luminescent material, respectively. [26]

$$\eta_{\mathrm{RA}} = \frac{1-\eta_{\mathrm{RAP}}}{1-\eta_{\mathrm{RAP}}\cdot\eta_{\mathrm{PL}}\cdot\eta_{\mathrm{Trap}}} \tag{5}$$

$$\eta_{\mathrm{RAP}} = \frac{\int_0^{\infty} d\lambda \int_{\theta_{\mathrm{Crit}}}^{\pi/2} d\theta \int_{-\pi/4}^{\pi/4} \sin\theta PL(\lambda)\left(1-\exp\left[-\varepsilon C\frac{Lt_0}{2t_0 \sin\theta\cos\phi}\right]\right)d\phi}{\int_0^{\infty} d\lambda \int_{\theta_{\mathrm{Crit}}}^{\pi/2} d\theta \int_{-\pi/4}^{\pi/4} \sin\theta PL(\lambda) d\phi} \tag{6}$$

In which η_{RAP} is the reabsorption probability, θ_{Crit} and θ are the critical angle and azimuth respectively, *C* is the concentration of the luminescent material, *L* is the plate length, ε is the molar absorptivity of the luminescent material, t_0 is the thickness of the waveguide in which the luminescent material is embedded, and ϕ is the in-plane rotation angle. [26]

2.2 Quantum Dots

Quantum dots, also known as artificial atoms, are a relatively new type of semiconductor material, first synthesised in good quality colloidal phase by *Bawendi et al.* in 1993 [27] and are semiconductor nanocrystals in the range of several nanometres. The most interesting properties of QDs originate from the quantum confinement effect, causing the E_g of the semiconductor to change as function of its size. Normally in the bulk phase the E_g of a semiconductor is fixed at a single value, depending on the material. When the particle size of the semiconductor decreases and starts approaching the exciton Bohr radius, the E_g increases. [28] [29] The exciton Bohr radius is the spatial extension of an exciton in the bulk material. The increase of the E_g arises from confinement of the exciton within the semiconductor nanocrystal, giving the exciton more kinetic energy. Figure 3 shows the optical effect of quantum confinement in CdSe. The graph at to bottom shows the emission spectra of several of the quantum confined CdSe nanocrystal samples. The quantum confinement affects the density of states (DOS) of the particles resulting in new electronical properties.

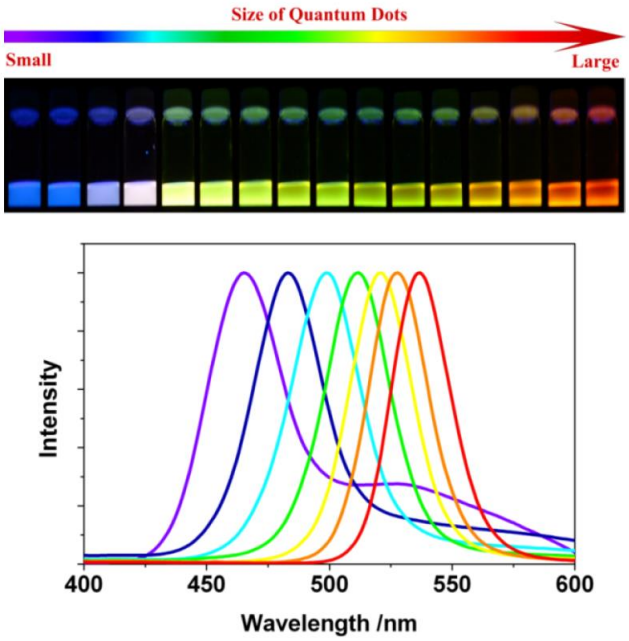

Figure 3: This image shows the quantum confinement effect in CdSe on the emission wavelenth. From left to right the confinement decreases, resulting in a decrease in E_g and will, therefore, increase in emission wavelength. Produced from [29].

Figure 4 shows a semiconductor, which is confined in several dimensions. It shows bulk material, a quantum well, a quantum wire, and a QD. The bulk material is not confined in any direction, while the quantum well and the quantum wire are confined. The quantum well is a 2-dimensional (2D) material, which is confined in one dimension, and the quantum wire is a 1-dimensional (1D) material, which is confined in two directions.

The QD is a semiconductor nanocrystal and is considered a 0-dimensional (0D) material. In this case the semiconductor nanocrystal is confinement in all 3 dimensions. Confinement in any number of directions introduce unique properties to the nanocrystal. The most important one being the introduction of size dependence of the E_g. The E_g is key in determining the wavelengths the QD is able to absorb. For LSCs, it is desired to synthesise QDs which absorb a large part of the solar spectrum and emit photons in the red to near infra-red (NIR) region. In this region, most PV cells are most efficient.

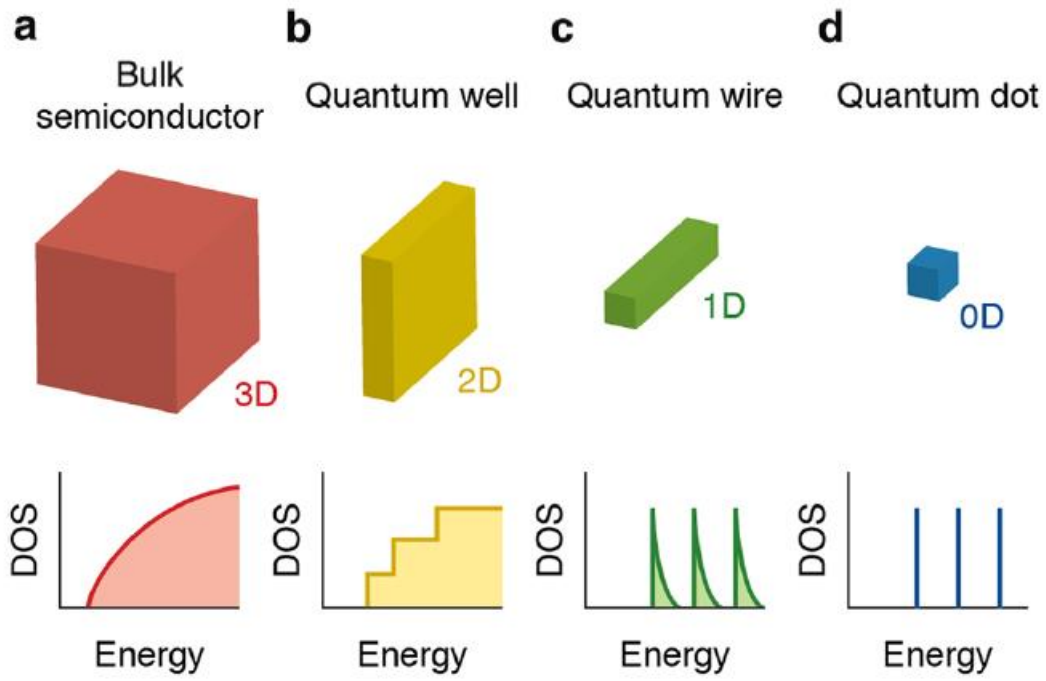

Figure 4:This image shows the effect of quantum confinement on the density of states. a) this image shows the DOS for an bulk semiconductor. b) A quantum well (2D material), which is confined in 1 dimension. c) A quantum wire (1D material), which is defined in 2 dimensions. d) A quantum dot (0D) material confined in 3 dimensions. Produced from [28].

A property unique to the QDs is the appearance of discrete energy levels upon confining the semiconductor material, as shown in graph of image d) of Figure 4. This property of discrete energy levels is similar to the discrete energy levels in an atom, therefore, the QDs are known as artificial atoms. The values of these energy levels can be calculated using wave functions and can constructed from a Bloch wave function (Ψ_{Bloch}) and an envelope wave function (φ_{env}), which are the wave functions of the bulk semiconductor and the confinement respectively. [30] The equation for this wave function is given in equation 7:

$$\Psi_{\mathrm{Total}}(x) = \Psi_{\mathrm{Bloch}}(x) \cdot \varphi_{\mathrm{env}}(x) \tag{7}$$

The φ_{env} is the solution to the Schrödinger equation of a "particle in a box", where the box is a spherical potential box rather than a cubic one, because QDs have the same confinement in all three directions and are, therefore, spheres. The φ_{env} can be described as the product of the spherical harmonic function and the radial Bessel function and is similar to the wave function of the electron in a hydrogen atom. This function is described in equation 8:

$$\varphi_{\mathrm{env}}(\theta, \phi, r) = Y_l^m(\theta, \phi) \cdot R(r) \tag{8}$$

In which Y_l^m is the spherical harmonics and *R(r)* is the Bessel function. The difference between the QD and the hydrogen atom is the positive charged core present in the hydrogen which is not present in the QD. For a hydrogen atom the potential changes inversely to the distance of the core, while the potential for the QD is the same throughout the QD but zero outside of the QD. Solving the Schrödinger equation for equation 8 yields the following equation:

$$E_{n,l}^{conf}(D) = \frac{2\hbar^2 \chi_{n,l}^2}{m^* d^2} \tag{9}$$

In which $E_{n,l}^{conf}$ is the solution to the Schrödinger equation for the discrete states, *d* is the diameter of the QD, $\hbar$ is the reduced Planck constant, m^* is the reduced mass of the charge carrier, and χ is a root for the Bessel function and is dependent on the principal quantum number (*n*) and Azimuthal quantum

number (*l*). Because of the difference in potential function between hydrogen and QD *l* is not restricted to $l \leq n$-1. Therefore, states like 1P are possible as well. This results in the discrete energy states visible in Figure 5.

The Schrödinger equation is now solved for the φ_{env}, which yields solutions only to the discrete energy states. To calculate the total bandgap (E_g^{total}), the solutions for the electron and the hole must be added to the bulk bandgap.

$$E_g^{total} = E_g^{bulk} + \frac{2\hbar^2 \chi_{n,l}^2}{m_{e^-}^* d^2} + \frac{2\hbar^2 \chi_{n,l}^2}{m_{h^+}^* d^2} \tag{10}$$

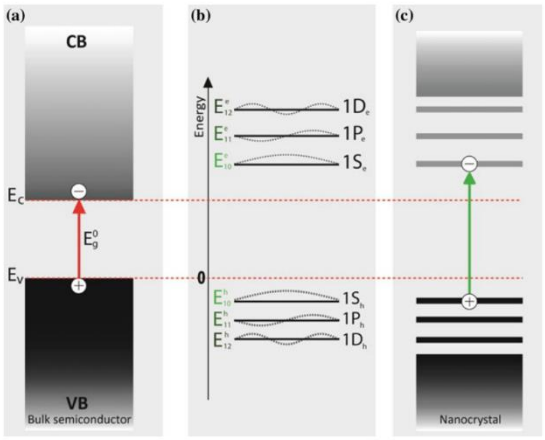

Figure 5: This image shows the bandstructure for bulk and quantum confined semiconductors ((a) and (c), respectively) and the determined discrete energy levels (b). Produced from [30].

There is more to tailor about QDs than just their size. Three other tailoring methods involve doping, alloying, and creating hetero semiconductor nanocrystals. The researched system in this thesis involves both doping and creating hetero semiconductor nanocrystals.

2.2.1 Doping

Doping is the intentional introduction of impurities in semiconductor crystals and was first introduced in the 1940s in bulk. [31] The impurities disturb the local band structures and create local states between the valance band (VB) and CB. In QDs, both light and heavy doping is possible with different kinds of doping, resulting in a broad range of possible doping affects. These impurities are present in the QDs as ions if the confinement energy is greater than the coulombic interaction between the dopant and charge carriers. The optical, electronic and magnetic properties of the QDs can be tailored by doping. Tailoring of QDs using doping does not only depend on the dopant, but on concentration and location of the dopant as well. [29]

2.2.2 Traps and passivation

By creating hetero semiconductor nanocrystals, the photoluminescent QY can be influenced. The definition of the QY is the ratio of photons emitted to photons absorbed and is limited by the non-radiative decay pathways. These non-radiative decay pathways exist due to defects in the QD lattice structure and dangling bonds at the surface structure. These non-radiative surface states have energy levels that generally lie between the VB and CB. [29] Therefore, they are able to trap charge carriers (electrons and holes) in these surface states, forcing non-radiative decay. Figure 6 shows the four pathways for exciton recombination. The desired pathway is depicted with arrow 1. In this case, the exciton directly recombines from the InP CB to the VB resulting in radiative recombination of the

exciton. The red arrows show undesired recombination pathways. These pathways are usually undesired, because the resulting emission is broad and redshifted or non-existent. However, not all trapped decay pathways are undesired, some are created intentional (e.g. doping). Arrows 2, 3, and 4 involve recombination of a charge carrier from and/or to a trapped state (red arrows). The orange arrows indicate trapping and relaxation processes. The trapping of charge carriers is a reversible process if there is enough energy to excite the charge carriers back into the band. This energy is usually thermal energy such as lattice vibrations (phonons). [32]

The defects, which create a trapping state, can occur all over the QDs, from vacancies in the middle of the core particle to the dangling bonds on the edge of the QDs. On the edge, the dangling bonds can occur in different facets of the nanocrystal, resulting in an even broader distribution of positions. These different positions result in a distribution of the energy of the trapped states, causing the broad trap emission.

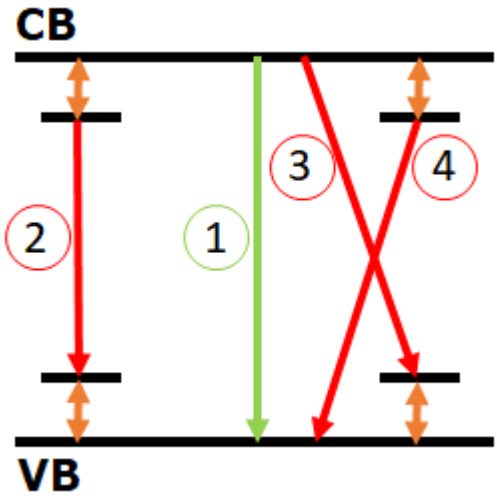

Figure 6: Possible decay mechanisms in QDs. The green arrow (1) is ussually the desired decay pathway, from CB to the VB. The red arrows (2), (3), and (4) are decay pathways utilizing trapped states, which usually broad and redshifted, or quenched emission. All the red arrows are decay pathways from and/or to trapped states. The orange arrows represent the trapping of the charge carriers, which can be a reversible process.

Therefore, passivation of dangling bonds is required. This passivation can be achieved using organic ligands, but this is not ideal. There are always leftover surface states and interaction between ligand and ion are weak enough to be broken by UV light. A better solution is to create hetero semiconductor nanocrystals by encapsulating the QDs with an inorganic shell to passivate the dangling bonds. [29]

Encapsulating QDs can lead to several different systems. Three of these systems are depicted in Figure 7, Type I, I½, and II. The difference between these systems composes entirely out of the size and positioning of the E_gs of the materials. Type I is a core-shell QD where the core has a smaller E_g than the shell material and the VB and CB of the shell lie below and above the bands of the core, respectively. This causes the electron and photon to be confined within the core material and, therefore, creates a large overlap between the wave functions of the charge carriers and has spatially direct excitation. Type II has a core particle with a VB and CB with energies higher than that of the shell material. In this material, the hole and electron both reside in different materials, in the shell and core respectively. Type I½ has one of the carriers localized in one of the materials, while the other is delocalized over both. [30]

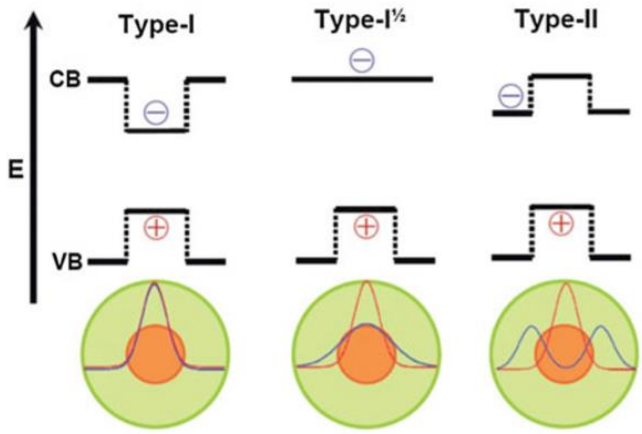

Figure 7: The three different Types of semiconductor heteronanocrystals with their wave functions and overlap. In Type I systems both the hole and electron are confined within the core of the particle. Type II systems have one charge carrier localized in the shell and the other charge carrier localized in the core. The Type $I^{1/2}$ system has one charge carrier localized in either the shell or the core, and one charge carrier delocalized over both the core and shell. Produced from [33].

Since Type I hetero nanocrystals confine both the charge carriers to the core, the exciton has little to no interaction with the surface traps of the shell. Therefore, the non-radiative decay and trap emission get reduced dramatically, resulting in a QY (often) higher than 50%. Due to spatially direct excitation in Type I hetero nanocrystals, the absorption and emission spectra are mostly unaffected by shell growth, disregarding the high energy peaks which appear due to the transitions entirely within the shell. Though the charge carriers are confined in the core, there will still be leakage of the charge carrier wave functions into the shell material. This is because the difference in E_g energy is finite and not infinite. [30]

The spatial separation of charge carriers in Type II systems lead to long lifetimes of the excitons, because wave functions have small overlap. In the case that the excited electron is trapped in CB of the shell, it means that the exciton has a great amount of interaction with trapped states from the cations near the CB. In the case that the hole is trapped in VB of the shell, that means that there is a large amount of interaction between the trapped states of the anion near the VB. Both cases result in decreased radiative emission.

Type $I^{½}$ systems have an intermediate amount of interaction with the surface traps. This is because one of the bands (VB or CB) carries a charge carrier, which is delocalized over both shell and core. This yields a QY somewhere in-between the Type I and Type II systems. Type $I^{½}$ are the result of small differences in E_g and/or by thin shells. [30] The absorption and emission spectra of these systems are not unaffected by shell growth, due the fact that a charge carrier is present in a growing effective core, therefore, a redshift occurs.

Figure 8 gives the bulk E_gs of semiconductor materials relative to vacuum level. These values could be used to get an idea of what materials to use, when encapsulating a QD. Other important parameters are crystal structure and lattice parameters, because these determine the likelihood of the success in encapsulation, and the efficiency at which the surface traps are passivated. It is easier to grow a shells with the same crystal structure as the core (e.g. zinc blende on zinc blende). This way, more dangling bonds of the core are passivated, because atoms are placed exactly where those dangling bonds are. The same structure continues from the core to the shell. The lattice constant is important, because it can cause a lot of strain and defects if the lattice constant of the core and shell are not similar. Alloys or intermediate layers can be utilized to transition between significantly different lattice constants of the core and desired shell. Examples are Cu^+:InP/ZnSe/$ZnSe_{1-x}S_x$/ZnS [20] and InP/GaP/ZnS. [34]

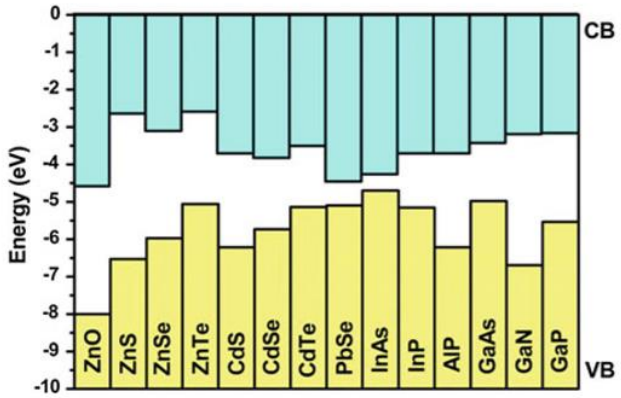

Figure 8: Bulk E_gs of several semiconducting materials. Though these are the bulk values, they can still give an indication of which materials to use to create the desired semiconducting heterocrystals on the nanoscale. Produced from [33].

2.3 Formation of nanocrystals

The size distribution of the QDs is an important aspect of the synthesis, due to the quantum confinement effect. If the size distribution is broad instead of narrow, the emission will be broad as well. This may not matter for the LSC, which utilize PV cells with equal efficiency over a large range of wavelengths, but does matter for other applications, such as phosphors in white LEDs. In order to achieve a narrow size distribution it is important to understand the different stages in the nanocrystal synthesis. Figure 9 depicts the LaMer plot, which shows the three stages of nanocrystal synthesis. The stages are monomer build-up (I), nucleation (II) and growth (III). For a narrow size distribution, it is important that the nucleation occurs in a very short time frame, which is needed to give every particle the same time to grow under the same reaction conditions. The term 'burst nucleation' is often used to describe this fast and homogeneous nucleation. [35]

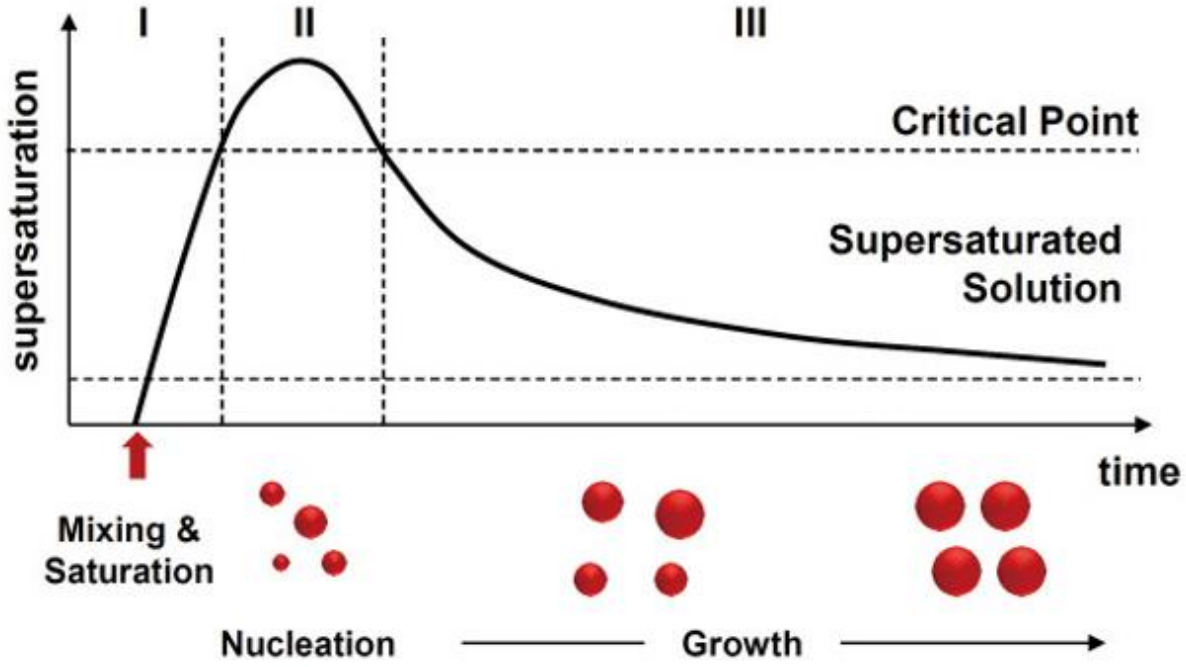

Figure 9: LaMer graph depicting the three stages of nanocrystal growth. Produced from [36].

2.3.1 Nucleation

The nucleation phase is the second phase in the nanocrystal synthesis (Figure 9) and can only occur once an energy barrier is surpassed. This energy barrier exists due to two different energies: volume free energy and surface free energy. [35] The volume free energy is the driving force for the nucleation of the nanocrystals and is described by equation 11:

$$\text{Volume free energy} = \frac{4}{3}\pi r^3 \Delta G_V \tag{11}$$

in which *r* is the radius of the forming particle and ΔG_V is the volume free energy per volume, which is negative in value. The ΔG_V can be described using equation 12:

$$\Delta G_V = -\frac{RT\ln(S)}{V_m} \tag{12}$$

in which *R* is the ideal gas constant, *T* is the temperature, *S* is the measure for the supersaturation of the monomer in solution, and V_m is the molar volume of the monomer in solution. [35] The volume free energy is counteracted by the surface free energy of the forming particle. This surface energy is given in equation 13:

$$\text{Surface free energy} = 4\pi r^3\gamma \tag{13}$$

in which γ is the surface energy. [35] Addition of the volume free energy and the surface free energy gives the total Gibbs free energy as function of radius, equation 14, and is plotted in Figure 10.

$$\Delta G = 4\pi r^3\gamma + \frac{4}{3}\pi r^3 \Delta G_{\mathrm{V}} \tag{14}$$

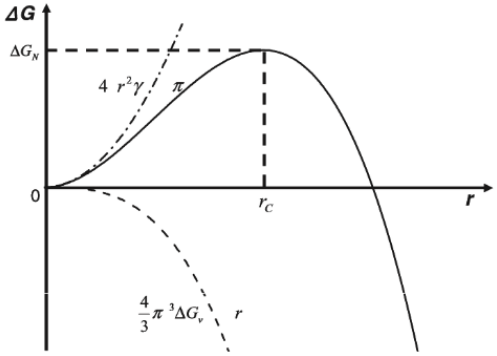

Figure 10: Plot of Gibbs free energy as function of the radius of the nucleus. The dashed and the dotted-dashed lines give the plots of the volume free energy and surface free energy, respectively. By addition of these lines, the solid line is achieved, which is the Gibbs free energy as function of the radius. Produced from [35].

By taking the derivative of equation 14 and setting it equal to zero the critical radius (r_c) can be found. Once this radius is reached the nucleation of the particle has occurred and growth starts. The critical radius can be calculated using the following equation [35]:

$$r_{\mathrm{c}} = \frac{2\gamma V_{\mathrm{m}}}{RT\ln(S)} \tag{15}$$

The Arrhenius equation can be used to determine the kinetics of the equation. [35] The activation energy is equal to the ΔG_{N}. By inserting equations 12 and 15 into equation 14, ΔG_{N} can be determined. This gives the following equation:

$$\frac{dN}{dt} = Ae^{\frac{-\Delta E_{\mathrm{a}}}{k_{\mathrm{B}}T}} = Ae^{\frac{-\Delta G_{\mathrm{N}}}{k_{\mathrm{B}}T}} = Ae^{\frac{-16\pi\gamma^3 {V_{\mathrm{m}}}^2}{3{k_{\mathrm{B}}}^3 T^3 {N_{\mathrm{A}}}^2 (\ln(S))^2}} \tag{16}$$

in which N_{A} is the number of Avogadro, A is a constant, and k_{B} is the Boltzmann constant. The temperature, supersaturation and surface energy are parameters, which can be controlled in experiments.

2.3.2 Growth

The growth of the nanocrystals can be split into two steps. Diffusion of the monomer to the growing nanocrystal is the first step in the growth. The second step is the reaction of the monomer on the surface of the nanocrystal. An equation for the monomer flux (the first step) can be created using Fick's law. By assuming, that the monomer flux is equal to the monomer consumption and by taking into account that there is a relationship between the monomer consumption and the volume change of the particle, the following equation can be constructed [35].

$$\frac{dr}{dt} = \frac{DV_{\mathrm{m}}([M]_{\mathrm{b}} - [M]_{\mathrm{r}})}{r - \frac{D}{k}} \tag{17}$$

In which $[M]_{\mathrm{b}}$ is the concentration of the monomer in solution, $[M]_{\mathrm{r}}$ is the solubility of a particle with a defined radius r, k is the reaction constant, and D is the diffusion constant. The growth of the nanocrystals can either be limited by the diffusion of monomer to the particle or by the surface reaction. [35] Equation 18 describes the case where the growth of the particle growth is restricted by

the surface reactions. This is applicable when D/kr>>1. Equation 19 describes the case where the growth is limited by the diffusion of the monomers to the particle. In this case, D/kr<<1.

$$\frac{dr}{dt} = V_m k([M]_b - [M]_r) \quad (18)$$

$$\frac{dr}{dt} = \frac{DV_m}{r}([M]_b - [M]_r) \quad (19)$$

Due to the Gibbs-Thomson relation, spheres have extra chemical potential, $\Delta\mu$, which can be expressed with the following equation:

$$\Delta\mu = \frac{2\gamma V_m}{r} \quad (20)$$

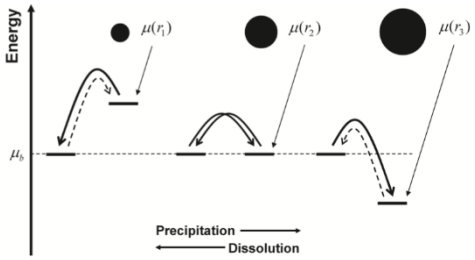

Figure 11: Principal of Ostwald ripening. Smaller particles have a higher chemical potential than the bulk solution and will therefore dissolve. Particles with a chemical potential lower than the bulk solution will grow using the monomers from the smaller nanocrystals. Produced from [35].

This chemical potential causes smaller nanocrystals to dissolve and bigger particles to grow (see Figure 11). This process, in which particles grow bigger by absorbing smaller particles, is called Ostwald ripening. Key features in the Ostwald ripening process are the reduction of particle concentration, particle growth occurs with a cube root over time, and an increase in the size distribution. [37] There is a seeming contradiction because the Gibbs-Thomson relation dictates that the smaller particles dissolve while bigger particles grow, while kinetics claim that smaller particles grow faster than larger particles. It can be concluded that the Gibbs-Thomson relation dominates when the radius of the particles is smaller than the critical radius and that kinetics dominate when r is bigger than r_{max}, where r_{max} is the radius at which the particles grow the fastest.

A process similar, yet opposite, to Ostwald Ripening was discovered in 1999 for metal nanoparticles called digestive ripening (or reverse Ostwald ripening). [38] Matter transfer from larger particles to smaller particles occurs during digestive ripening, narrowing the size distribution of the ensemble. [39] [40] Models to explain the mechanism behind digestive ripening to an satisfactory extend have yet to be produced. A theory *Lee et al.* [41]has been proposed based the assumption of charged colloidal nanoparticles which describes the effect well, however experiments show that not only the charge matters. Ligands seem to play an important role in this process, especially alkylthiols, alkylamines, triphosphines, and alkylsilanes seem to promote digestive ripening. [42] It is suggested that Ostwald and digestive ripening are part of the same phenomenon. [39] Digestive ripening has been successfully performed on the synthesis of CdSe and CdTe as well. [43]

2.3.3 Hot-injection and heat-up methods

Generally, two methods are utilized to obtain burst nucleation. These are the hot-injection method and the heat-up method. Both methods yield nanocrystals of high size uniformity. These methods have been utilized in order to synthesise a large range of different semiconductor nanocrystals, with a large range of different materials and sizes. Also the shape of the nanocrystals are tuneable with these methods.

Hot-injection entails the rapid injection of a ‘cold’ precursor into a hot and rapidly stirring precursor. Usually the cold injected precursor is the cationic precursor and the hot precursor is usually the anionic precursor. The hot precursor temperature is often around 300-350 °C before the cold precursor is injected into the reaction mixture. After injection of the cold precursor, the first phase of Figure 9 starts, the monomer build up. This is typically a fast reaction, which is quickly followed by the second phase, the nucleation. The nucleation occurs when the temperature and supersaturation are still high enough to from nuclei. The supersaturation and temperature quickly decrease after the formation of the first nuclei, making further nucleation impossible. At decreased temperature and monomer concentration the synthesis enters the third phase of the synthesis, the growth phase. The growth occurs using the monomers left in solution as well as the monomers coming from the smaller crystals. The other method is the heat-up method. This method also results in the synthesis of highly monodisperse nanocrystals. This method entails the preparation a (cold) reaction mixture. This mixture is quickly heated to the reaction temperature. Though at first glance, one would not expect suspect burst nucleation to occur using this method, experimentally it occurs. The burst nucleation is likely due to build-up of intermediate product. Both methods rely on ligands to stabilize the particles in the solution. The concentration and chemical structure of these ligands have influence of the size and shape of the resulting particles. Examples of ligands are myristic acid and oleic acid. Hot-injection is used during the experiments in this thesis.

2.4 Copper-doped Systems

Copper doped systems are desired for applications such as LSCs. The copper causes a large effective stokes shift in materials such as InP and thus reduces reabsorption of emitted photons. In this section, multiple copper doped systems are discussed, because there are few papers published about copper-doped indium phosphide itself. These systems include not only QDs, but bulk semiconductors and copper based metal-organic complexes as well. [44]

Figure 12A shows a copper doped bulk semiconductor. In this case, it is ZnS doped with Cu^{+} and Al^{3+}. The band diagram shows the excitation of an electron from the VB to the CB. The hole in the VB will be trapped at the copper ion and the excited electron will become partially confined around the aluminium ion. Recombination of the hole and excited electron results in photoluminescence with red-shifted light. The copper ion is usually located in a zinc ion vacancy. Because the copper ion (1+) has a different charge than the zinc ion (2+) this has to be compensated with another ion, in this case the aluminium ion is used. The copper and aluminium are a donor-acceptor pair (DAP), where the hole is trapped in the copper ion, and the electron is partially localized around the aluminium ion, resulting in a small overlap in wave functions. Therefore, there is slow decay of the trapped exciton. These systems have strong electron-phonon coupling resulting in broad emission bands with a full width at half maximum (FWHM) of 300 meV. [44]

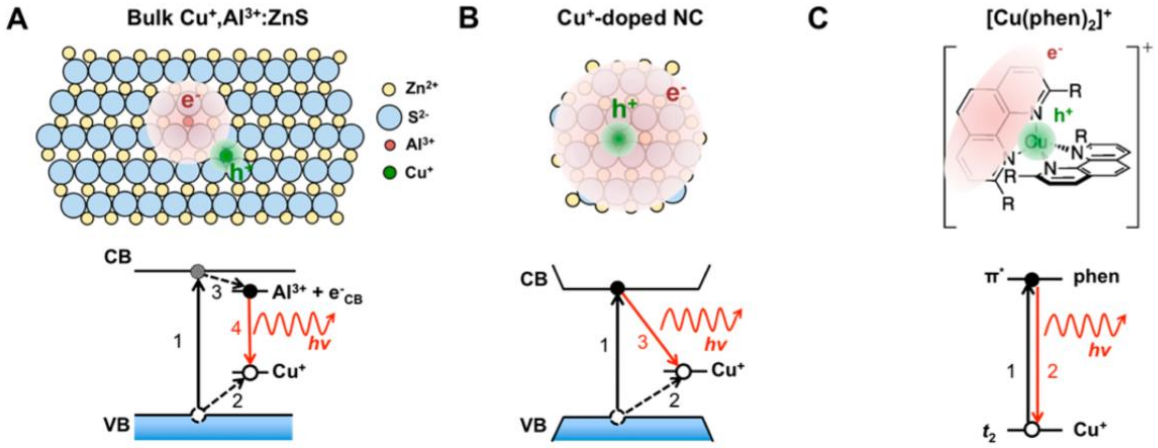

Figure 12: A) This image shows a copper-doped bulk semiconductor and its band structure. The bulk system uses Al^{3+} to form a DAP with Cu^{+}. B) This image shows a copper-doped semiconductor nanocrystal and its band structure. C) This image shows a copper-based metal-organic complex and its molecular orbitals. In all the images, the holes are trapped in the green areas, while the electrons (de)localized on the pink areas. Produced from [44].

Figure 12C shows an example of a copper-based metal-organic complex, Cu^{+} bis(phenanthroline). In this complex an electron is excited from the t_2 state of the copper ion to the π^{*} state of one of the ligands, leaving a Cu^{2+} ion. The excitation of an electron utilizing this process is called metal to ligand charge transfer (MLCT). Within a picosecond after the excitation of the electron, the complex is subjected to Jahn-Teller distortions. These distortions reduce the symmetry of the metal-organic complex from D_{2d} to D_2. This complex has a broad FWHM for the emission due to the rearrangements of the complex, 380 meV, and has short lifetimes compared to the bulk semiconductor (0.05– 5 µs). [44]

Figure 12B shows the system with most relevance pertaining this research, a Cu^{+} doped QD. Both the bulk and QD system trap the holes in the Cu^{+} ions (after trapping Cu^{2+}), but differ for the electron. While the bulk systems localizes the electron in the Al^{3+}, the QD system has partially delocalized electron due to quantum confinement. This creates a much larger overlap of the electron and hole wave functions, resulting in shorter lifetimes than the bulk semiconductor (see Figure 12B). The excited state of the doped QD system is very similar to that of the metal-organic complex. During the excitation of the electron, it is excited to the CB of the QD, while the hole is trapped upon the copper

level. The CB in this case acts like π^* of the ligand in the metal-organic complex, while the Cu^{2+} acts as the metal. This excited state could, therefore, be described as a $ML_{CB}CT$. The resulting recombination is, therefore, a ligand (CB) to metal charge transfer ($L_{CB}MCT$). Electron-phonon coupling results in a broad FWHM for the emission. In the these copper doped QD systems the energy of the copper energy levels fixed relative to vacuum. [44] The emission is tuneable through the CB, by changing the nanocrystal size (see Figure 13). Density functional theory suggests that there are some minor energy variations in the copper acceptor level energy, because of hybridisation between 3d copper orbitals and anionic p orbitals from the VB. [44]

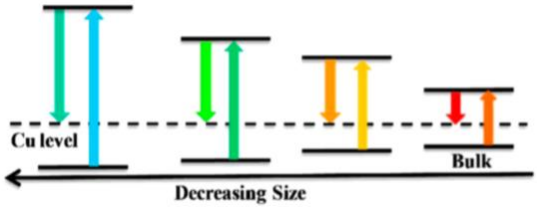

Figure 13: This image shows the effect of quantum confinement on the emission of a Cu^+-doped nanocrystal. Produced from [44]

Tananaev et al. performed research on the effect of copper dopant in CdSe QDs. [45] This research shows that the luminescence of the first excitonic peak emission decreases and the down-shifted emission increases when the copper dopant concentration increases in the CdSe. Figure 14 shows the photoluminescence spectra. 1 has the lowest copper dopant concentration (0 %) and 7 has the highest copper dopant concentration (0.5 %). Similar experiments were performed by *Yang et al.*, who performed the measurements on higher copper concentrations (0.075 to 0.6 Cu^+:Cd^{2+} ratio). [46] At higher copper concentrations the copper induced emission did not change significantly.

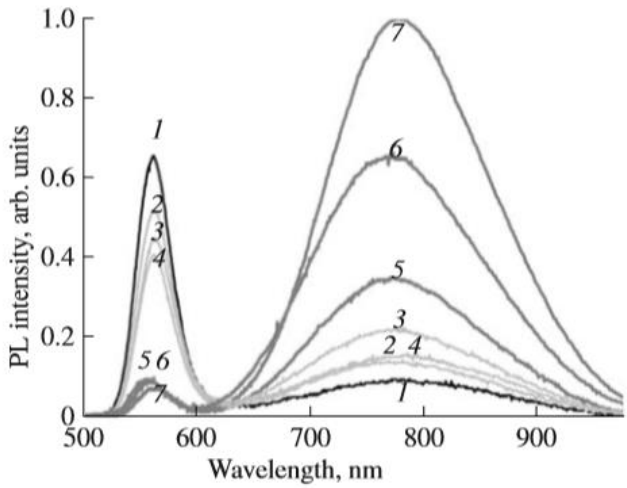

Figure 14: This figure shows the effect of copper doping concentrations upon CdSe QDs. At lower wavelengths is the first exciton emission and at higher wavelengths are the dopant induced emission and trap induced emission. The dopant range is from 0 to 0.5% copper (1 to 7, respectively).Produced from [45].

There are conflicted opinions on the oxidation state of the copper ion in the semiconductor nanocrystals. Synthesis of these systems are most often performed using Cu^{2+} to dope the QDs, but many scientist claim the copper ion is present as Cu^+. Other scientist claim it already is 2+ before photo-excitation. Several experiments have been performed to confirm the oxidation state of the copper ion. Electron paramagnetic resonance (EPR) confirms the presence of Cu^+. When comparing the optical properties of the copper-doped QDs with Cu^+ and Cu^{2+} doped bulk InP, it is determined that the InP is doped with Cu^+. This reduction of copper most likely occurs by electron rich solvents and ligands. [20] [44]

Emission of the Cu^{+}-doped QDs has a broad FWHM (see Figure 14). *Knowles et al.* give in their review FWHMs for several different copper-doped QD systems. [44] Determined is that these systems have FWHMs of 200 to 600 meV and it is caused by strong-electron phonon coupling.

2.5 Indium Phosphide

Research in QDs have mostly been focussed upon II-VI and IV-VI systems, such as CdSe and PbS, respectively. Lately, the attention has been shifted to research in the more covalent III-V semiconductor QDs. There are several advantages to using these III-V systems, such as low toxicity and high optical stability. One of the major disadvantages is the rather challenging syntheses for these systems. [47] [48] Another drawback arises due to the covalent bonds of these materials, which are difficult to analyse using techniques like transmission electron microscopy (TEM), because the covalent bonds are easily destroyed under the high-energy electron beam. Finally, there is also strong size quantization effects, causing relatively large FHWM in absorption and emission spectra. [48]

Among the the III-V QDs, InP has good qualities for the LSC application. As shown in Figure 8, InP has a relatively small E_g. The E_g of the bulk material is 1.35 eV (918 nm), which corresponds to NIR light. Introducing nano-dimensionality to the bulk InP it can be tailored to absorb and emit anywhere in the visible spectrum. [47] [48] Therefore, InP QDs can be used to absorb a great part of the solar spectrum. The drawback concerning the broad FWHM of the emission spectrum is not relevant for LSC applications, because the PV cells inside are built to effectively absorb photons over a large range of wavelengths. InP has a zinc blende crystal structure with a lattice constant of 5.87Å.

2.5.1 InP quantum dot synthesis

Typically, InP QD synthesis involve either a hot-injection or a heat-up synthesis. The most widely studied synthesis for InP is a hot-injection synthesis, developed by *Battaglia et al.* in 2002. [49] In this synthesis, an indium carboxylate salt (e.g. indium myristate or indium palmitate) is dissolved in a high-boiling point non-coordinating solvent (e.g. ODE). This mixture is heated to 300 °C and injected with the phosphor precursor, containing Tris trimethylsilyl phosphine ($P(TMS)_3$). After injection at 300 °C, the temperature is set at 270 °C for growth.

The $P(TMS)_3$ agent is utilized, because the P^{-3} can be used directly, without the necessity for oxidation or reduction reactions. The disadvantage to using this phosphor precursor lies in its reactivity. This phosphor precursor is too reactive, causing the phosphor precursor to deplete almost immediately at injection. The 3 steps in the LaMer diagram (Figure 9) occur simultaneously, reducing the range of possible sizes obtainable by varying reaction time. Experiments with different phosphor containing agents have been performed. Experiments utilizing mixtures of $P(TMS)_3$ with similar phosphor containing agents (e.g. Triarylsilylphosphine) show some success. [50]

During the research for this thesis, an altered version of the synthesis of *Xie et al.* is performed. [22] The synthesis of *Xie et al.* and the synthesis of *Battaglia et al.* are very similar. The main difference between these syntheses is the addition of a small amount of octylamine to the phosphor precursor before injection. This small amount of octylamine allows the injection- and growth temperature to be lowered to 188 °C and 178 °C, respectively. *Xie et al.* utilizes ODE and octylamine to dilute the $P(TMS)_3$ before injection, however, during this research tri-octylphosphine (TOP) is used instead of ODE.

According to *Allen et al.* the octylamine suppresses the depletion of the $P(TMS)_3$ by solvation. [51] It is proposed that at the start, the $In(MA)_3$ is coordinated to the octylamine in the exterior solvation sphere. During the first reaction (in Figure 15) $P(TMS)_3$ is integrated into the solvation sphere, forming complex 1. This reaction is reversible. Next, the $In(MA)_3$ loses a MA group (intermediate state in Figure 15) before the phosphor agent loses a TMS group forming complex 2. Finally, complex 2 will convert to InP. This process inhibits the depletion of the phosphor precursor.

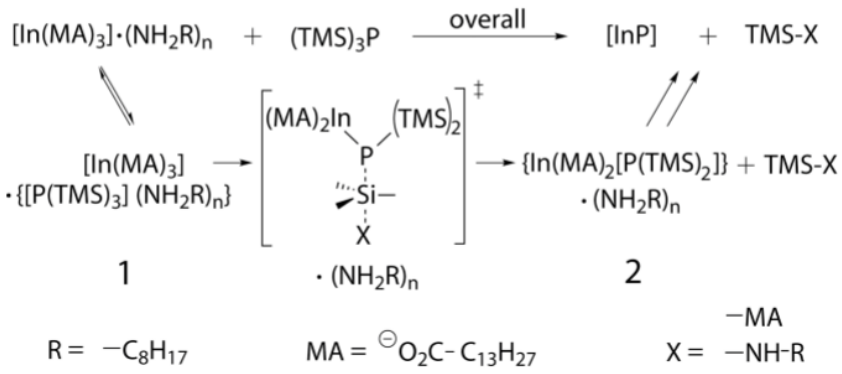

Figure 15: Mechanism for inhibitation of dopant depletion, where the alkylamine coordinates around the In precursor to slow down the reaction. Produced from [51].

The injection temperature decrease is possible due to a mechanism proposed by *Cossairt*. [52] It is proposed that the InP QD synthesis proceeds due to the formation of magic size clusters (see Figure 16). It takes a lot of energy to progress the magic size cluster to a full QD. The addition of a primary amine disturbs these magic size clusters resulting in a lower energy barrier to overcome to continue growth. Therefore, there is less thermal energy (heat) needed to progress the growth in the presence of octylamine.

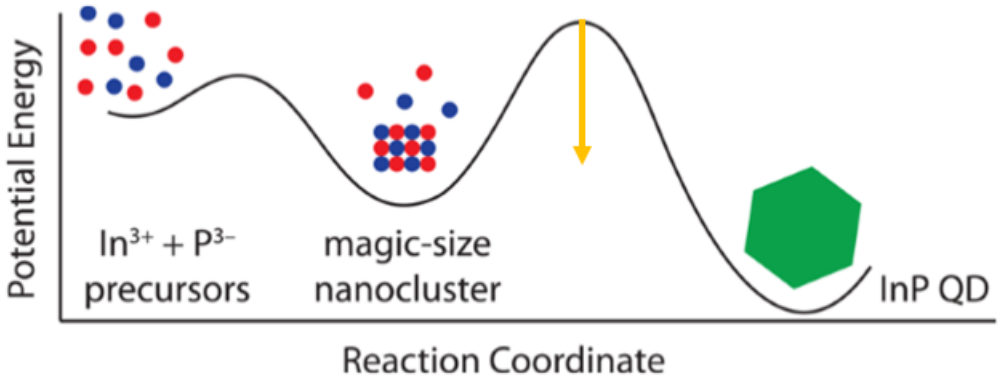

Figure 16: This graph shows the energy barriers in the formation of InP QDs. The energy barrier between magic size nanoclusters and QDs can be reduced by the introduction of primary alkylamines such as octylamine, as shown by the orange arrow.Produced from [53].

TOP is used because *Harris et al.* discovered that it slows the reaction. The higher the concentration TOP present, the slower the reaction, which is similar to the effect of octylamine. [53] Furthermore, the TOP may be an extra source of phosphor and thus might be able to extend the growth range of the particle without sacrificing the size uniformity.

2.5.2 Size and concentration

To increase the QY a shell is grown around the QDs. When utilizing the successive ionic layer absorption and reaction (SILAR) technique, it is necessary to calculate the exact amount of shell material needed. To calculate these values, the size and concentration of the particles are needed. In the thesis of *Ministro*, a sizing curve for InP QDs is given (equation 21). [47]

$$E_g = 1.35 + \frac{1}{(0.119 \pm 0.003) * d^3} \quad (21)$$

d represents the diameter of the InP QDs in nm and 1.35 eV is the E_g of bulk InP. The absorption coefficient is utilized to determine the concentration of the QDs, however, the bulk value of the InP

absorption coefficient is not the same as the absorption coefficient for InP QDs. Values for InP QDs can be calculated using the equations below by *Ministro*. [47]

$$\varepsilon_{335} = 4.40 * 10^4 * d^3 \quad (22)$$

$$\varepsilon_{410} = 1.29 * 10^4 * d^3 \quad (23)$$

In which ε is the absorption coefficient at a wavelength of 335 nm and 410 nm in $\frac{\mathrm{L}}{\mathrm{cm \cdot mol}}$.

To calculate the amount of material to grow 1 monolayer of shell, the volume of the shell of certain particles must be calculated. The calculated volume is divided by the volume of a unit cell of shell material. In a zinc blende unit cell, there are 4 anions and 4 cations. Multiply the number of ions (cations or anions) by the particle concentration to get the necessary amount of shell material.

2.5.3 Cu^+:InP quantum dots

Little research has been performed on Cu^+:InP QDs. [22] [20] As explained earlier, InP is a great luminescent material for LSCs, since it is able to absorb a significant portion of the solar spectrum. However, it still has a large overlap between the absorption and emission, causing reabsorption of emitted photons. This causes significant losses in LSC efficiency. Doping the InP with Cu^+ reduces the overlap between the absorption and emission, thus reduces the reabsorption losses. The overlap is reduced due to a down-shift of the energy of the absorbed photon, using the $ML_{CB}CT$ excited state (see Figure 17A), which results in down-shifted emission. [20] A comparison of InP and Cu^+:InP is given in Figure 17B. [22] The top graphs show emission from InP QDs with several different particle sizes. The bottom shows Cu^+:InP with similar particle sizes. Clearly large down-shift occurs, but also a severe broadening of the peaks occur upon doping.

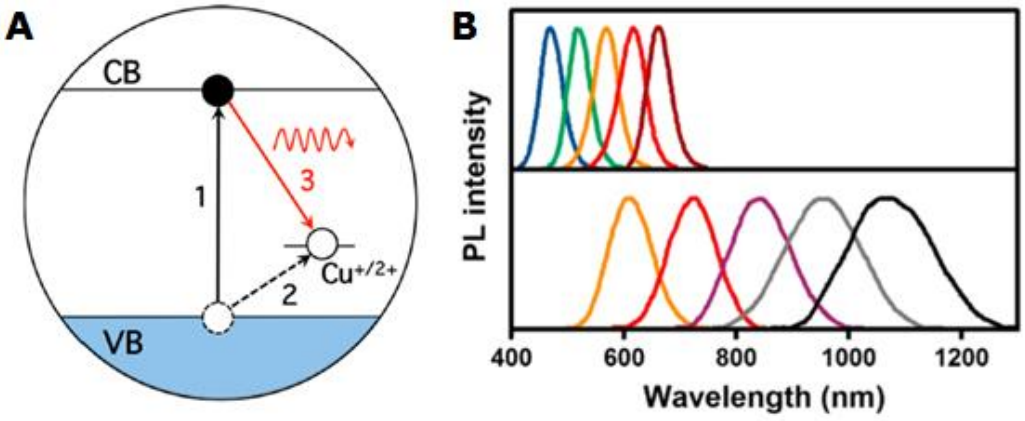

Figure 17: A) This figure shows the emission mechanism of Cu^+:InP QDs. [20]. B) These graphs show emission for undoped (top) and doped InP (bottom) for nanocrystals within the same size range. Produced from [22].

Differences in mechanisms between bulk and QD Cu^+:InP exist. In case of the bulk material, the excited electron is trapped into either a donor induced defect or in an acceptor ion (in case of DAP). In QDs this is not the case. Acceptor ions are ruled out because there are no acceptor ions present. Donor induced defects are ruled out because the emission wavelength changes with the CB of the QD. [20]

In the research of *Knowles et al.* it is shown that ternary semiconductor nanocrystals such as $CuInS_2$ are very similar in decay mechanism to Cu^+:InP and Cu^+:CdSe systems. All the materials show broad emission bands and large effective stokes shifts. They all three show the same magnetic-exchange and zero field splitting between singlet and triplet states. It is concluded that their excited-states are indistinguishable. [20]

Another difference between the bulk and QD Cu^+:InP systems is the mobility of the copper ion within the lattice. [22] The critical temperature of diffusion of copper ions within QDs is 230 °C, while in bulk 580 °C. This lowered critical temperature of diffusion creates a problem in which the dopant copper ions can easily be ejected out of the InP lattice. This 'lattice ejection' even occurs at temperatures lower than 100 °C for Cu^+:ZnSe. [54] The lattice ejection in Cu^+:InP QDs can be avoided by encapsulation with ZnSe. The ZnSe acts as an diffusion barrier for the copper ions, since it has the same crystal structure with smaller lattice parameters. [22] Even better would be an $ZnSe_{1-x}S_x$ shell, because ZnS has smaller lattice parameters. The $ZnSe_{1-x}S_x$ encapsulation would also serve a second purpose. The creation of a Type I QD, which has far higher QY than just Cu^+:InP cores, making the system better for LSCs.

2.6 Transient absorption spectroscopy

Transient absorption (TA) spectroscopy is a characterization technique, which takes absorption spectra of an (partially) excited system at specific moments in time. A pump pulse promotes a portion of the system to the excited-state at the start of the measurement, which is followed by a weak probe pulse of white light, occurring at a predetermined delay (τ). The absorption spectrum of the excited system is taken utilizing this probe pulse. The difference in absorption spectra between ground-state and excited-state are calculated by subtracting the absorption spectrum from the ground-state from the absorption spectrum of the excited-state (ΔA). By varying the τ over a range in time, a spectrum can be constructed for ΔA as function of wavelength (λ) and τ, which gives information about mechanisms of energy transitions occurring in the measured system. [55]

The calculated ΔA(λ,τ) spectrum shows features due to several processes, including ground-state bleaching. When the pump pulse promotes the electrons to an excited-state, the transitions to this excited state are no longer possible, resulting in a negative ΔA upon subtracting the ground-state absorption spectrum from the excited state spectrum. Stimulated emission is another process contributing to the ΔA, pertaining the emission of a photon when the probe pulse journey through the sample, which only occurs for allowed transitions and is Stokes shifted regarding the aforementioned ground-state bleach. The effect of the stimulated emission is a negative ΔA and is weak compared to the effect of the ground-state bleaching, because the pulse of the probe is weak compared to the pulse of the pump, therefore there are a lot more excited states than stimulated emissions. Excited-state absorption is another process contributing to the ΔA spectrum, entailing a possible transition which becomes possible after the system is promoted to its excited-state and causes, unlike the previous processes, a positive ΔA. [55]

There have thus far been no reported papers in which TA measurements are performed on Cu^+:InP. However, there have been papers on TA measurements with Cu^+:CdSe and Cu^+:CdSe/CdS, by *Maiti et al.* and *Hughes et al.* respectively. [56] [57] It is observed that the cooling of the hot-electron in Cu^+:CdSe occurs at a slower rate than in CdSe, 0.7 ps and 0.4 ps respectively and is due to prevention of Auger cooling if the hole is trapped upon a copper trap, though the rate remains within the sub ps regime. Another effect of trapping the hole upon the Cu^+ seems to be an inhabitation of external quenching by hole acceptors in the solvent. Lastly, TA measurements have shown L_{VB}MCT absorption in the excited state, which occurs because an electron is able to get excited from the VB to the Cu^{2+}.

3 Materials and methods

As stated before, the Cu^+:InP/$ZnSe_{1-x}S_x$ QDs were chosen because this luminescent material has the potential reduce reabsorption within LSC applications. InP QDs are able to absorb light up to 600 nm, a sizable part of the solar spectrum, and the presence of copper dopant down-shifts the photons to red-NIR light, using the $ML_{CB}CT$ excited state. This down-shift prevents the reabsorption by other QDs in the LSCs, thereby greatly reducing losses in LSCs. $ZnSe_{1-x}S_x$ shells are grown on the QDs to improve the QY and trap the Cu^+ ion inside the QD. During this research Cu^+:InP/$ZnSe_{1-x}S_x$ QDs were synthesized, before they are characterized.

The research was conducted in three main steps:

1. The synthesis of Cu^+:InP/$ZnSe_{1-x}S_x$ QDs.
    a. InP core synthesis.
    b. Copper doping of InP cores.
    c. Growing a shell around the cores.
2. Varying the shell thickness.
3. Varying the copper dopant concentration.

3.1 Synthesis of Cu^+:InP/$ZnSe_{1-x}S_x$ QDs

In the first step, the Cu^+:InP/$ZnSe_{1-x}S_x$ QDs were synthesized, this was divided in 3 parts. The first part involved the InP core synthesis, utilizing a hot injection synthesis. The hot-injection synthesis started with the preparation of the indium(III) myristate ($In(my)_3$) precursor using indium acetate, myristic acid, and octadecene (ODE). This was mixture was degassed under vacuum on a Slenck line at 120°C. After degassing, the precursor was moved into a glovebox, was heated to 188°C, before a phosphor precursor containing TOP, octylamine, and $P(TMS)_3$ was injected. After 30 minutes of growth at 178°C the reaction was quenched with ODE. The synthesized cores are characterized using absorption spectroscopy.

Following the core synthesis, was the post-synthesis doping. In this part, the InP cores were doped with copper utilizing a post-synthesis doping method, which involves the dropwise addition of copper(II)stearate ($Cu(st)_2$) at 130°C. After the addition, the reaction mixture was heated from 130°C with a rate of 1°C / minute until 220°C was reached. Copper diffused into the InP lattice during this heating process. After the Cu^+ doped QDs were synthesised, the QDs are characterized utilizing both absorption and emission spectroscopy.

The final part consisted of the encapsulation of the Cu^+:InP cores in a $ZnSe_{1-x}S_x$ shell, which was performed by addition of $Zn(st)_2$, and the addition of TOP-Se and/or TOP-S at 150°C after 15 minutes of stirring, depending on the desired sub shell. After the addition of the precursors, the mixture was heated to 220°C for 30 minutes, before it was cooled down. This was performed for each sub shell. The fully synthesized QDs are characterized using absorption and emission spectroscopy.

A more detailed protocol of the synthesis is presented in appendix 2.

3.2 Varying shell thickness

Optimizing the QY through shell thickness variation was the second step of this research. During this step, several monolayers of shell were grown around the QD cores, varying in thicknesses of 3, 5 and 7 monolayers of shell material. The shells were grown utilizing SILAR and consisted of ZnSe, $ZnSe_{1-x}S_x$ and ZnS, in this order. ZnSe and ZnS have a large lattice mismatch, making it difficult to grow these materials upon one other. Therefore, there was always 1 monolayer of $ZnSe_{1-x}S_x$ between the ZnSe and ZnS. SILAR requires an exact amount of shell material per monolayer, therefore, calculations were performed utilizing absorption spectra, the sizing curve, and the absorption coefficient, as explained in section 2.5.2.

The variations shown in Table 1 were performed for both doped and undoped InP QDs. During this research, a single batch of InP was split into four, subsequently, three of these four batches were used for encapsulation, while the other one was used as bare reference.

Table 1: Shell variation performed in this research.

Total number of monolayers	ZnSe monolayers	$ZnSe_{1-x}S_x$ monolayers	ZnS monolayers
3	1	1	1
5	2	1	2
7	3	1	3

The effect of varying the shell thickness is characterized using absorption and emission spectroscopy. In the shell optimization experiments a standard concentration of $Cu(st)_2$ was added during the doping phase, 0.008 M.

3.3 Varying copper concentration

The third and final step was the variation of the copper dopant concentration. Samples with various amounts of copper dopant were synthesized to get more insight in effect of the copper doping in the sample. This was achieved by varying the concentration of the $Cu(st)_2$ added during the post-synthesis doping method, while the volume of the added $Cu(st)_2$ solution always remained the same. Volume was kept the same, so that there was roughly the same concentration QDs present during each step of the synthesis for every experiment. In this research the following concentrations were used:

1. 0.001M
2. 0.002M
3. 0.004M
4. 0.007M
5. 0.008M*
6. 0.011M
7. 0.012M

During this research, a single batch of InP was split into four, subsequently, three of these four batches were used for doping, while the other one was used as undoped reference. These QDs with different copper concentrations were characterized using absorption and emission spectroscopy, and inductively coupled plasma optical emission spectroscopy (ICP-OES).

* Standard concentration used in the initial synthesis and shell thickness experiments.

3.4 Characterization

This research utilizes several characterization techniques:

1. Absorption spectroscopy
2. Emission spectroscopy
3. ICP-OES
4. TEM
5. Transient absorption spectroscopy

3.4.1 Absorption spectroscopy

Absorption spectroscopy determines several properties of the QD solution. The peak position and FWHM give information about the size and size-distribution, respectively. Using the absorption coefficient (at specific wavelengths), it is possible to calculate the QD concentration in the sample.

Absorption measurements were performed using a PerkinElmer LAMBDA 950, which is capable of measuring from 190-3300 nm, which accounts for the ultraviolet (UV), visible (VIS), and near infrared (NIR). This spectrophotometer has a deuterium and a tungsten lamp as light source, each for a different part of the measuring range. The generated beam of light is monochromised by a double monochromator (holographicgrating monochromator with 1440 lines/mm at240 nm and 360 lines/mm at 1100 nm), before the beam in split in two by the chopper. Each beam travel through a different cuvette (sample and reference), before where it is partially absorbed. The transmission difference between the two cuvettes is converted in to absorption. During these measurements, the range used was 300-750 nm and 300-1300 nm, for InP and Cu^{+}:InP respectively. Measurements were performed with a step of 1 nm with a broadness of 2 nm. For an average measurement, three cuvettes were prepared, one containing sample diluted by toluene (first absorption peak at ± 0.1 absorbance), and two contained pure toluene. The two pure solvents are used to measure the background spectrum, after which one cuvette with toluene is replaced with the diluted sample.

3.4.2 Emission spectroscopy

Emission spectroscopy gives information about the amount of photons emitted and their energy. This technique is important in determining the luminescent QY and the down-shift of the QDs. The lifetime of the excitons can also be determined from emission spectroscopy.

Emission spectroscopy was performed using USB4000-FL-395 and a Edinburgh Instruments FLS920 fluorescence spectrometer. The former was a small CCD with blue (395 nm) LED with a 400 nm long pass filter, which was used for quick emission measurements. Measurements were performed with an integration time of 1 second and an average over 5 measurements was taken. The latter (FLS 920) was used for was used for determining the QY and for time resolved emission measurements (TRES). The FLS920 utilized a 450 W Xe lamp and a Hamamatsu R920 photomultiplier tube (PMT) for emission measurements. For TRES, an optical parametric oscillator (OPO) laser was used as excitation source and a Hamamatsu H74220-60 PMT for detection.

Samples diluted similarly to absorption spectroscopy were used for the emission and TRES measurements. For determining the QY, a diluting series was made from the sample and a known dye.

3.4.3 ICP-OES

ICP-OES provides insight of the chemical makeup materials and is used to determine the copper doping in the QDs. The equipment utilized is the PerkinElmer Optima 8300DV spectrometer. Before the measurement, the QDs were washed 3x with toluene, acetone, and ethanol (1:1:16), during the third washing step 25 µL butylamine was added to remove stearates. The sample was dissolved in 64% HNO_3, diluted to 5% HNO_3 with water, and further diluted with 5% HNO_3 until the concentration of indium was 1%.

3.4.4 Transient absorption method

TA measurements are performed in order to gain more insight into the decay mechanisms of the exciton in the Cu^+:InP.

The utilized excitation source is a 800 nm laser (Mai Tai Ti:S oscillator), giving pulses of 110 fs. The output is amplified utilizing a regenerative amplifier (Spitfire Ace, Spectra Physics), of which 5% is used to generate white light utilizing CaF_2 (for probe pulse). The remaining 95% is doubled in frequency to 400 nm and is used as pump pulse. The light of the probe transmitted through the sample is measured using a CCD.

3.5 Chemicals

Name	Supplier	Additional information
1-octadecene	Sigma Aldrich	Technical grade, 90%, degassed before use
Acetone	Sigma Aldrich	Acetone dried (max. 0.0075% H_2O) SeccoSolv®, used as bought
Butylamine	Sigma Aldrich	99.5%, used as bought
Ethanol	Alfa Aesar	Alcohol reagens, anhydrous, denatured, 94-96%,used as bought
Indium(III) acetate	Sigma Aldrich	99.99%, used as bought
Myristic acid	Sigma Aldrich	99-100%, used as bought
Octylamine	Sigma Aldrich	99%, was degassed under vacuum of antechamber of glove box for a minute
Selenium	Fisher Scientific	Powder, 200 mesh, 99.5%, used as bought
Sulfur	Sigma Aldrich	99.98%, used as bought
Toluene	Alfa Aesar	99.8%, used as bought
Trioctylphosphine	Sigma Aldrich	97%, used as bought
Zinc stearate	Sigma Aldrich	Technical grade, used as bought

4 Results and discussion

In this chapter, the results of this research are presented and discussed. Similar to the method section above, the results are split in 3 parts:

1. Synthesis of the Cu^+:InP/$ZnSe_{1-x}S_x$ QDs.
2. Variation in the shell thickness.
3. Variation in the Cu^+ dopant concentrations.

After the three parts, there is a fourth part pertaining one of the TA measurements performed upon the Cu^+:InP/$ZnSe_{1-x}S_x$ QDs.

4.1 Synthesis of the Cu^+:InP/$ZnSe_{1-x}S_x$ QDs

In this first section, the results of the initial synthesis are presented and discussed. Starting with the synthesis of the InP core particles, which is followed by the post-synthesis doping and the shell growth.

4.1.1 Synthesis of the InP cores

Aliquots were taken during the InP synthesis to monitor the growth of the QDs. The aliquots were taken at 1, 5, 10, 20, 30, 40, 50, and 60 minutes after in injection of the phosphor precursor. Figure 18A gives the absorption spectra of the aliquots, showing one peak and one shoulder per spectrum, which are the peaks of the S and P transitions, respectively. The reaction time increases from purple to red, the purple line represents the spectrum of 1 minute and the red line represents 60 minutes. The S transition absorption peak is clearly distinguishable in all spectra, while the shoulder of the P transition absorption shows up twenty minutes after injection. Over time, the peak of the S transition redshifts to lower energies at a decreasing rate, showing a redshift from 2.47 eV to 2.33 eV for the 1 minute and 60 minute aliquots, respectively.

From this information, several deductions can be made. Small particles are highly quantum confined, resulting in a large E_g and a S transition absorption peak at high energies. Upon growth of the QDs, the confinement is reduced. Therefore, red-shifting the absorption peaks towards lower energy. This redshift is observed, indicating growth of the QDs. The fact that the rate of the redshift decreases over time, alludes to a decreasing growth rate over time. The appearance of the P transition absorption peak at t>20 minutes, indicates that the peaks become more narrow, which means that there is size focussing.

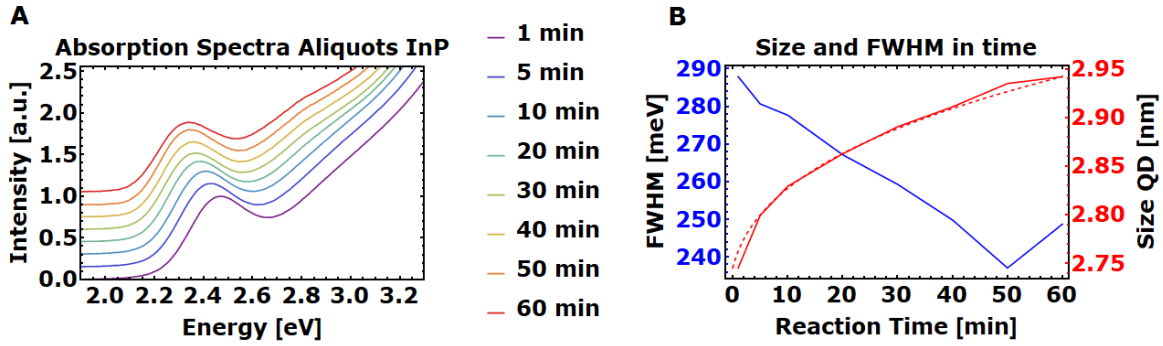

Figure 18: A) Absorption spectra of aliquots of the core synthesis taken at 1, 5, 10, 20, 30, 40, 50 and 60 minutes, from purple to red, respectively. B) FWHM (blue) and QD size (red) over time during core synthesis.

Figure 18B shows a decreasing FWHM and an increasing QD size over time, the blue and red lines respectively. The QD size was determined using the sizing curve from *Ministro et al.* and increases from 2.75 to 2.95 nm over the course of an hour. [47] The FWHM decreases from 290 to 240 meV.

The growth displayed in Figure 18B was fitted (Equation 24) and shows that the diameter of the QDs during this reaction increases with a cube root, which is a characteristic feature for Ostwald ripening. [37].

$$d = 2.68 + 0.0678 * \sqrt[3]{t} \quad (24)$$

In which 2.68 nm is the suspected particle size at t~0 and the 0.0678 nm/min$^{1/3}$ is a measure for the growth speed. To confirm the claim of Ostwald ripening, it is necessary to keep track of the particle concentration in each aliquot. This requires to take exact amounts of reaction mixture during a work-intensive synthesis. Sadly, this was not achieved. Theoretically, Ostwald ripening is a good fit for the hot-injection InP synthesis. The $P(TMS)_3$ precursor used is an extremely reactive precursor, which means that within seconds after injection it is depleted, leaving only Ostwald ripening to facilitate growth. Literature mentions that a hot-injection synthesis of InP utilizes Ostwald ripening as well. [58]

The decreasing FWHM, however, indicates that the growth is not due to Ostwald ripening, because Ostwald ripening increases the size distribution, resulting in larger FWHM. This decrease can be due to several reasons. First, larger QDs experience a smaller change in confinement when the radius is slightly increased (or decreased) compared to smaller QDs. Therefore, smaller QDs with a certain size distribution will have a larger FWHM, than larger QDs with the same size distribution, consequently, growth while keeping a certain size distribution results in a smaller FWHM. The more likely possibility is that the FWHM decreases due to size focussing, which means that Ostwald ripening is not the correct mechanism for this synthesis.

Digestive ripening is a better fit for this synthesis, because it is size focussing. As mentioned in the theory section, Ostwald ripening and digestive ripening are part of the same phenomenon, which could explain why growth occurs with a cube root of time. Another reason why digestive ripening is more likely than Ostwald ripening, is the presence of octylamine and TOP, which promote digestive ripening. [42]

4.1.2 Doping and encapsulation in shell

After the core synthesis, the cores were doped with copper ions, which was followed by encapsulation within a shell. Absorption and emission spectra are taken from four different samples:

1. InP
2. InP/$ZnSe_{1-x}S_x$
3. Cu^+:InP
4. Cu^+:InP/$ZnSe_{1-x}S_x$

These four samples were all synthesized from the same batch of InP cores. Figure 19 shows the normalized absorption and emission spectra. The solid lines represent the absorption spectra and the dashed lines the emission spectra. There is no emission spectrum present for the InP cores, because surface traps cause significant non-radiative losses resulting in weak emission. [59]

In Figure 19 a few features are worth mentioning. There is a redshift in the absorption spectra upon encapsulation of the QDs in a shell. This is observed in both InP and Cu^+:InP, from blue to green and black to red respectively. The energy of the redshift of both InP and Cu^+:InP is comparable (± 150 meV). Note that the absorption features of the first excitonic peak severely diminish upon doping with copper and that a copper "tail", extra absorption at lower energy, appears. The most obvious change in the emission spectra is between the undoped and doped QDs, showing a large redshift, ±600 meV, between the emission of undoped and doped QDs. The difference between the FWHM of the bare and encapsulated Cu^+:InP is 460 and 350 meV respectively, while the FWHM of the InP/$ZnSe_{1-x}S_x$ is 225 meV. Note that the overlap of the absorption and emission decrease significantly if the sample is doped.

The redshift in absorption spectra for encapsulated QDs is due a reduction in quantum confinement, which means growth of the effective core. This reduction in confinement is, therefore, most probably due to leakage of charge carriers from the InP to the ZnSe. This is possible because the CBs of both materials are relatively close to each other in energy. The Cu^+ doping does not seem to affect this redshift since both doped and undoped systems experience similar redshifts (± 150 meV).

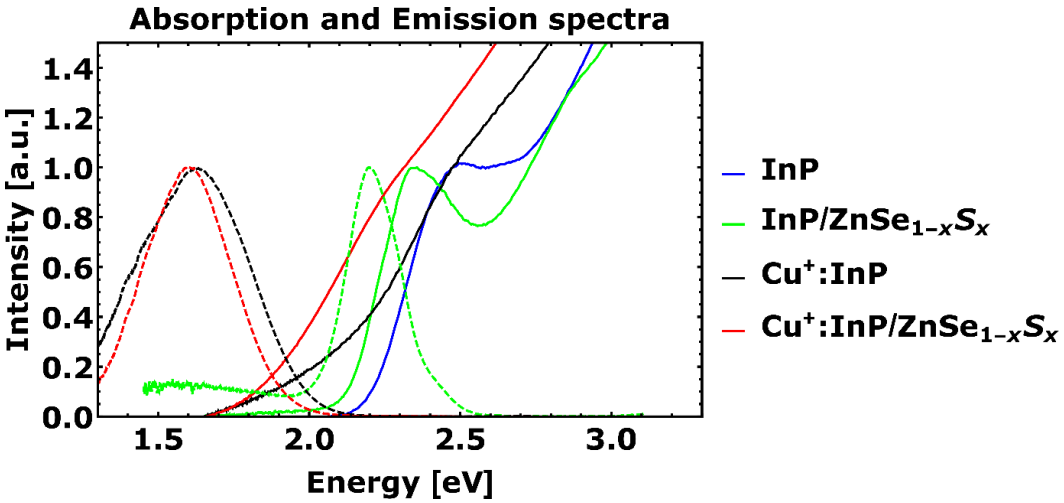

Figure 19: Absorption and emission spectra taken from (un)shelled of (un)doped QDs, solid and dahsed line respectively. Note the redshift in the absorption upon encapsulating (green and red) compared to the bare QDs (blue and black). The downshifting in the emission is observed for the Cu^+ doped QDs (black and red) and not in the emission of the undoped InP (green). Emission is measured with a CCD with an excitation wavelength of 395 nm and a 400 nm long pass filter.

The presence of the tail in the absorption spectra of the Cu^+ doped QDs is due excitation of electrons from the Cu^+ to the InP CB ($ML_{CB}CT$). This excitation occurs with light of lower energy than the S transition because the energy gap between the Cu^+ level and the InP CB is smaller than the E_g of the InP QDs. The loss of features within this absorption peak is most likely due to a combination of the,

suspected interstitial, copper doping and the $ML_{CB}CT$ copper absorption. The loss of features is more thoroughly discussed in section 4.3.2, where the copper dopant concentrations are varied.

The observed redshift of the emission after the doping process is due to $L_{CB}MCT$ decay pathway, as discussed in the theory section, and is desired. The reduction in reabsorption is shown in Figure 19 by the reduced overlap between absorption and emission. In the undoped system (green) this overlap is ±60%, while in the Cu^+ doped systems (black and red) this is reduced to ±10%.

The FWHM of the emission changes significantly for each system. Most notable is the difference between the doped and undoped systems, which have a FWHM of 225 and ±400 meV respectively. The 400 meV is due to strong electron-phonon coupling. There is a smaller difference between the FWHM of the bare and the shelled doped QDs, 460 and 350 meV respectively. There are two possibilities for the difference in FWHM. The first possibility might give insight on the position of the Cu^+ ions in the QDs. Close to the surface of the InP cores, the lattice is less rigid and more easily influenced by phonons or the $Cu^{+->2+}$ charge changes. Upon growing a shell around the QDs with $ZnSe_{1-x}S_x$, the core may become slightly strained, because this shell material has smaller lattice parameters. Therefore, the edge of the InP core becomes more rigid and is less influenced by phononic vibrations and charge changes. This reduces the fluctuations in crystal field strength upon the emission in this phonon coupled emission, thus reducing the FWHM of this emission peak. The second possibility is that the encapsulation eliminates trap emission processes, which can broaden the FWHM, because not all traps are at the same energy.

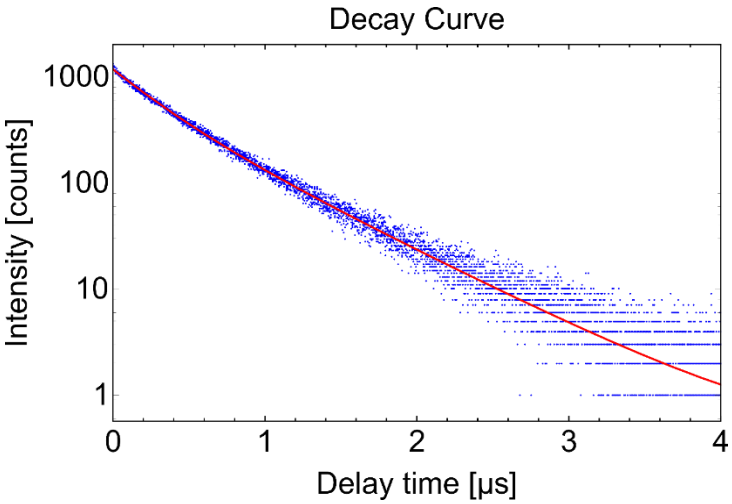

Figure 20: This histrogram depicts the decay curve of the exciton and is used to determine the lifetime of the exciton. It was fitted with the redline, which has a bi-exponential decay. The fit gives two lifetimes of 0.27 and 061 µs, which both account for 50% of the emission. The sample was excited with 657 nm (OPO) laser and 10 µs pulse.

Figure 20 shows the histogram of the arrival time of the photons upon the detector after recombination of an exciton in the Cu^+:InP/$ZnSe_{1-x}S_x$ QDs. The blue dots give the decay curve of the QDs and the red line is the fit of this decay curve.

The decay curve has a bi-exponential fit meaning that there are two lifetimes: 0.27 µs and 0.61 µs, which is within the same order of magnitude as *knowles at al.* observed. [20] Both account for 50% of the processes. Since the lifetimes are both in the hundreds of nanoseconds and trapping occurs within picoseconds, it can be stated that both decay processes (with 0.27 µs and 0.61 µs) involve the hole trapped upon a Cu^+ dopant. Another argument for the involvement of copper is that the lifetimes are much too long to occur without involving the Cu^+ ion. The lifetime of similar (undoped) InP systems are around 40 ns, which is an order of magnitude lower. [60]

The fact that the decay curve is fitted with a bi-exponential decay curve hints at two processes. It is possible that there are separate processes for Cu^+ ions within the tetrahedral holes and the octahedral

holes of the InP lattice. However, the fact that the line can be fitted with a bi-exponential does not necessary mean that there are actually two processes. There is no theoretical reasoning behind exponential fits. Another model was tried as well, in which the copper dopant distribution was taken into consideration, however, this failed to give a good fit as well.

4.2 Variation in the shell thickness

This section shows the results of the effects of shell growth on the photoluminescent QY. Using the SILAR method shells were grown around both undoped and doped InP QDs. Each shell consists of 3 components in that order (see Figure 21):

1. A number of ZnSe monolayers
2. A single $ZnSe_{1-x}S_s$ monolayer
3. A number of ZnS Monolayers

Shells consisting of 3, 5 and 7 monolayers were grown. First, the undoped InP QDs are addressed, followed by the Cu^+ doped InP QDs.

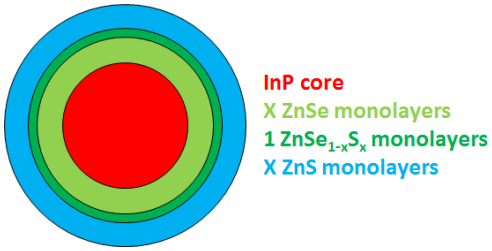

Figure 21: Schematic cross-section of a fully encapsulated QD with 3 sub shells. There are an X number of ZnSe and ZnS monolayers, and 1 $ZnSe_{1-x}S_x$ monolayer in between.

4.2.1 Encapsulated InP QDs

During this this experiment shells were grown around the undoped InP QDs and included 3, 5, and 7 monolayers of shell material. Aliquots were taken during the synthesis of the sample with 7 monolayer shell. Absorption and emission measurements are performed upon the samples with 3, 5 and 7 monolayers of shell material and on the aliquots as well.

Emission spectra of the undoped InP QDs with 3, 5 and 7 monolayers of shell

The results of the emission measurement show that the emission increases when increasing the shell thickness from 3 to 5 to 7 monolayers worth of shell material (Figure 32 in appendix 3). This is expected, because upon growing a single layer of shell (Type I), most traps on the surface of the core are passivated, causing an increase in luminescence. However, electrons are still able to tunnel into trap states on the interface of the shell. Therefore, upon increasing the shell thickness, the chance of tunnelling into the trapped states on the surface are reduced and the luminescence increases. Another possibility is that during shell growth, the QD grew bigger than the wave function of the electron, thereby, cutting the electron off from non-radiative decay pathways on the surface states.

Aliquots from the encapsulation of the undoped InP QDs with a 7 monolayer shell

Figure 22 gives more information on the encapsulation process. Aliquots were taken during the growth of the 7 monolayer shell and are characterized using absorption and emission spectroscopy. Figure 22A shows the absorption spectra of the aliquots and bare InP (red). By growing a single monolayer around the bare InP QDs there is a redshift in the S transition absorption peak from 2.25 to 2.275 eV, for each following peak the redshift is smaller and constant. The P transition absorption peak appears around 2.6 eV when growing thicker shells.

The large redshift in the absorption spectrum from bare- to encapsulated InP QDs (single monolayer) indicates reduced quantum confinement, meaning that the effective core of the QD has grown. This

could be either from actual growth or from leakage of the exciton into the shell. Since this particular redshift is significantly larger than the redshift between the other monolayers of shell, it is unlikely that redshift comes only from leakage of electrons into the shell. It possible that the core has grown before the first shell is grown, digestive ripening is a possible mechanism for this growth, because the cores are not (yet) protected by the shell. Another explanation for the larger redshift upon the growing the first monolayer, is the fact that solvent is replaced by a shell. Therefore, the infinity energy barrier of the solvent is replaced by the finite barrier of the shell, allowing a larger relaxation of the wave function. The smaller redshifts occurring upon the stacking of shells are also due to electrons leaking into the shell.

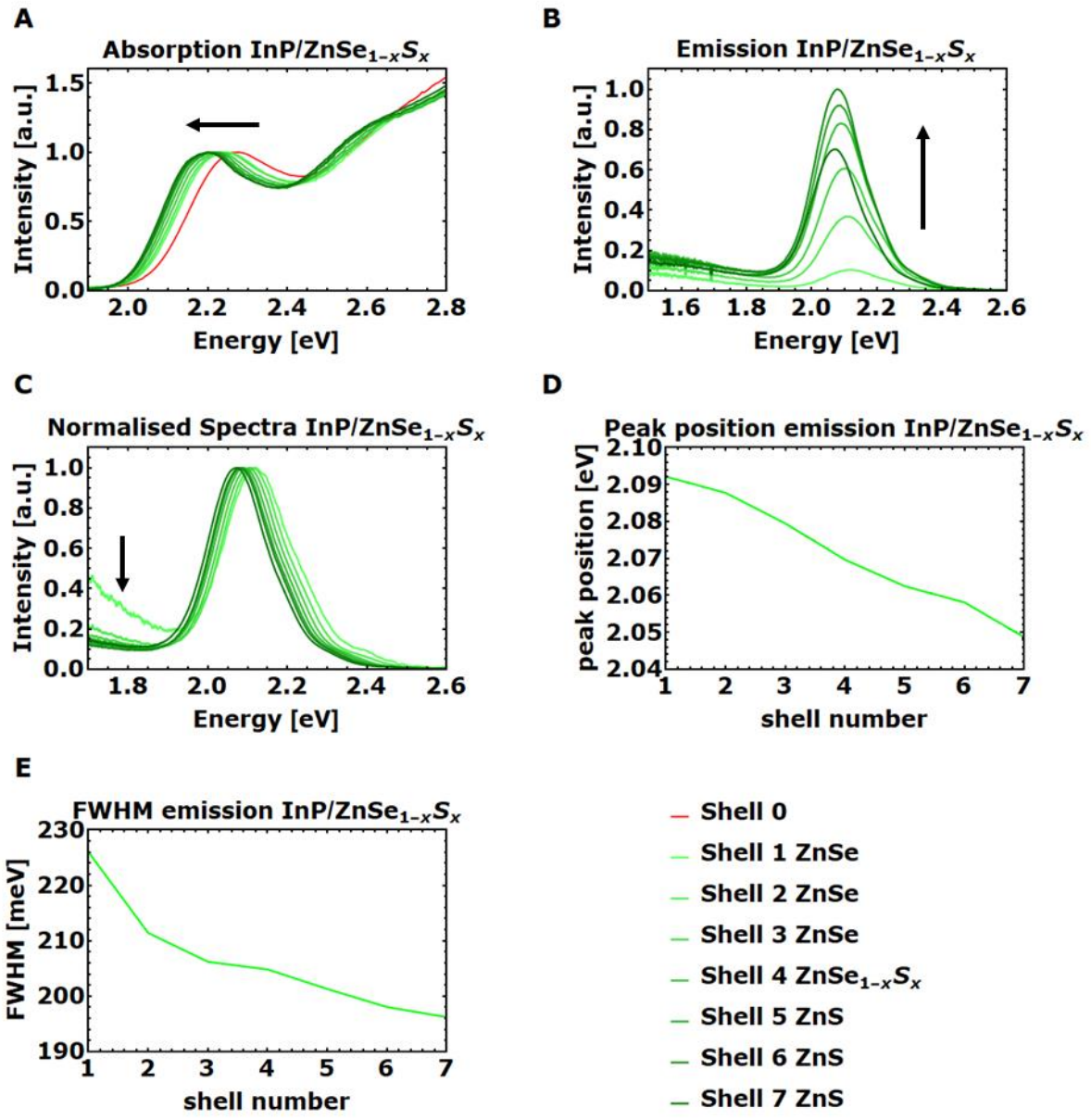

Figure 22 These graphs give the results of the absorption and emission measurements performed on the aliquots, which were taken during the synthesis of the 7 monolayer shell in the encapsulation experiment of undoped InP. A) This graph shows the absorption spectra with the absorption peaks of the S and P transistions for each newly grown monolayer. B) This graph shows the emission intensity for each newly grown monolayer. C) This graph shows the normalised spectra of the emission peaks. D) This graph shows the redshift in the peak position of the emission peaks. E) This graph shows the FWHM of the emission as functino of the number of monolayers in the shell.

Figure 22B shows the emission spectra of the aliquots. In this graph the emission is normalized with the maximum emission intensity of the 6 monolayer aliquot. The emission intensity increases with each consecutive monolayer except for the 7th (and final) monolayer. This 7th monolayer has emission with an intensity between the the 3rd and 4th monolayers. The FWHM of the emission spectra is ± 200 meV. The spectra show emission at energies lower than 1.9 eV.

The most notable result from the emission spectra measurements is the drop in intensity after the final monolayer is added to the QDs (Figure 22B). The trend is that each added monolayer increases the luminescence of the QDs, however the 7th monolayer does not seem to comply with this trend. Instead of increasing the luminescence, it decreases the luminescence significantly. There are several reasons why the spectrum from the 7th monolayer should be ignored. Apart from the fact that the emission intensity of the 7th does not comply with the trend, this aliquot was measured at a different day, which makes it unreliable. The emission intensity seems to increase the most upon growth of the ZnSe monolayers, which is unexpected. ZnS should give the highest increase inemission intensities, because it gives a Type I heterostructured QD, instead of a Type I½ like the ZnSe. However, this is not observed. It is likely that the ZnS shell is not thick enough to form a Type I QD.

Figure 22C shows the normalized emission spectra of the aliquots, which shows that there is emission at energies lower than 1.9 eV for all spectra and this emission is strongest for the single monolayer aliquot. Note that the intensity of this emission is roughly the same as for all the other samples.

The emission in Figure 22C at energies below 1.9 eV has lower energy than the E_g, therefore, this observed emission is trap emission. The relative intensity of the trap emission decreases when more shell material is added, indicating that this trap emission mostly originates from surface traps. The reduction, but not disappearance, of the trap emission could have several explanations. It could indicate that due to the lattice mismatch not all surface traps are passivated, leaving InP surface traps for trap emission. Another possibility is that the electron tunnels through the shell to a surface trap on the surface of the shell, this chance of tunnelling decreases with increasing shell thickness. The final possibility is that there are radiative traps inside the InP core. A combination of all three possibilities is most likely.

Figure 22D shows a linear relation between the emission peak position and the shell thickness, which can be fitted with a linear equation. Equation 25 gives a linear fit, in which *x* is the number of monolayers of the shell and *P* is the peak position.

$$P = 2.132 - 0.0083x \tag{25}$$

From this fit, it can be concluded that with each shell the peak position redshifts with ±8 meV. This should not occur for the ZnS monolayers (monolayer 5, 6 and 7), because the ZnS monolayers are utilized in order to create Type I heterostructured QDs. In type I QDs, the electrons do not leak into the shell and, therefore, a redshift is not expected. There are two possible explanations for this observation. It is possible that there is alloying between the ZnSe and ZnS, resulting in an alloy in which electrons might be able to leak. The second possibility is that the ZnS shell is too thin to form a true Type I heterostructured QD and, therefore, electrons will be able to tunnel through the ZnS shell into surface traps.

Figure 22E shows the FWHM of the encapsulated QDs, which decreases upon an increasing shell. This is likely due to the shells constraining the QDs, resulting in a narrow size distribution for the cores. With each layer the strain should increase less, which is observed in the decreasing rate of narrowing in the figure.

4.2.2 Encapsulated Cu^+:InP QDs

After the encapsulation of undoped InP cores, the Cu^+:InP were encapsulated in a $ZnSe_{1-x}S_x$ shell. Research into the encapsulation of Cu^+:InP was performed similarly as in the InP. Monolayers of ZnSe, $ZnSe_{1-x}S_x$ and ZnS were grown around the doped QDs and shells of 3, 5, and 7 monolayers were grown and aliquots were taken during the synthesis of the 7 monolayer sample. After synthesis the samples and aliquots are characterized using absorption and emission spectroscopy and the QY is measured for the samples of 5 and 7 monolayers.

Emission spectra and QY of the Cu^+:InP QDs with 3, 5 and 7 monolayers of shell

The emission spectra from the encapsulated Cu^+:InP QDs with 3, 5 and, 7 monolayer shells show similar results (Figure 33 in appendix 3) as seen in the encapsulation of the undoped InP QDs. The luminescence increases upon increasing the shell thickness, which is seen in the undoped InP as well. The QY of the 5 and 7 monolayer samples were measured using a dilution series of the samples and a dilution series of the reference dye (12% QY). Absorption and emission measurements of the dilution series were performed, obtaining the graphs shown in appendix 3 (Figure 34). Using the following equation the QY was determined:

$$QY_{sample} = QY_{Dye} * \frac{slope\ QD\ dilution\ series}{slope\ Dye\ dilution\ series} * \frac{{n_{QD}}^2}{{n_{Dye}}^2} \quad (26)$$

Where n_{QD} and n_{Dye} are the refractive indices of the solvent of the QDs and Dye respectively. This gives QYs of 21 and 26%, for the 5 and 7 monolayer samples respectively.

Aliquots from the synthesis of the Cu^+:InP QDs with 7 monolayer shell

During the encapsulation of the 7 monolayer shell around the Cu^+:InP QDs, aliquots were taken. These aliquots are characterized, utilizing absorption and emission spectroscopy. Figure 23 shows the spectra of the aliquots taken during this synthesis. Figure 23A depicts the absorption spectra of the aliquots, including bare, doped and undoped QDs. Similar to Figure 19, upon doping with Cu^+ the absorption the FWHM severely broaden and features disappear. Upon shell growth, the absorption peak of the sample redshifts significantly. Figure 23B depicts the emission spectra of the aliquots, showing, that there is a significant down-shift between the absorption and the emission. The emission peaks reside at 1.45 eV and have a large FWHM (335 meV). Compared to the absorption, there is a smaller redshift in the peak position for the emission. Figure 23C and D show the peak position and FWHM of the emission respectively, as function of the monolayers of the shell.

The observed redshift in the absorption indicates an increase of the effective core size, which is similar to the undoped sample discussed above. This increase is created due charge carriers leaking into shell after the growth of the shells. The loss of features will be discussed in chapter 4.3.2

The observed down-shift between the absorbed and emitted photon is due to the $ML_{CB}CT$ excited state, as discussed in chapter 4.1.2. The emission intensity increases as function of the amount of monolayers shell material, similar to the results of the undoped InP encapsulation experiment (Figure 22C). The addition of ZnSe monolayers has greater effect upon the luminescence than the addition of ZnS monolayers. More experiments are needed to determine the cause of this is the effect.

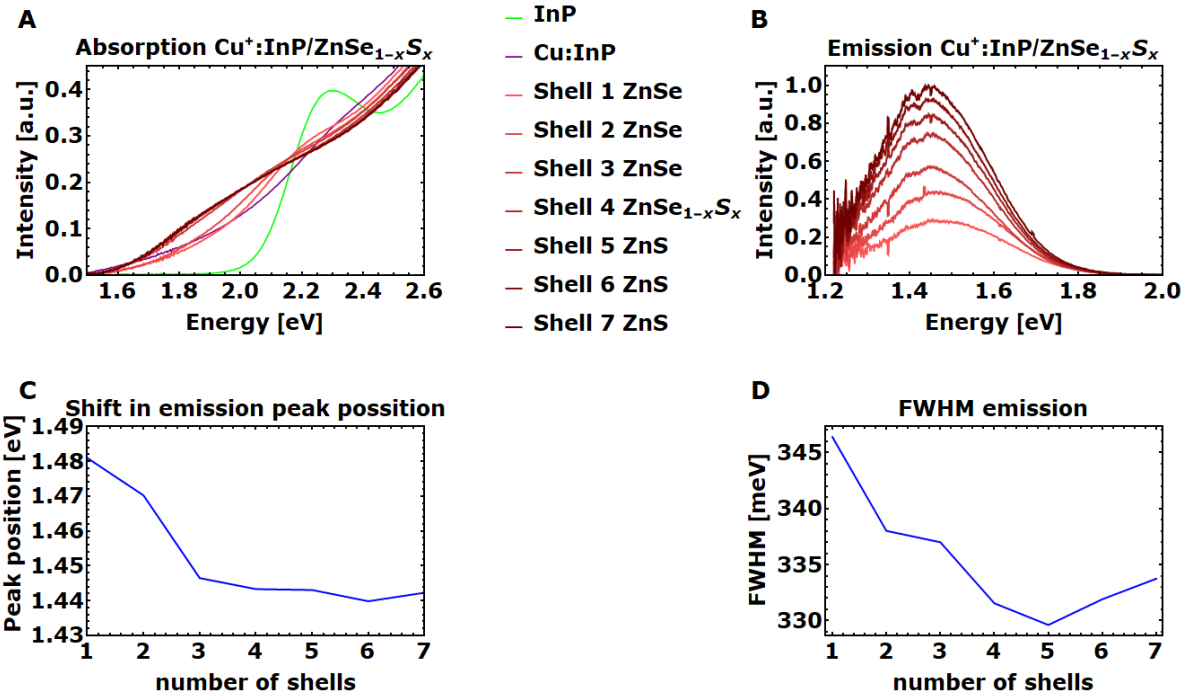

Figure 23: These graphs give the results of the absorption and emission measurements performed on the aliquots, which were taken during the synthesis of the 7 monolayer shell in the encapsulation experiment of Cu⁺:InP. A) This graph shows the absorption spectra with the absorption peaks for the S transistion of each newly grown monolayer. B) This graph shows the emission intensity for each newly grown monolayer. C) This graph shows the redshift in the peak position of the emission peaks. D) shows the FWHM of the emission as function of the wavelength.

Due to the loss of features, it is not possible to determine the exact redshift in the absorption peak position (Figure 23A). Otherwise, an absorption redshift twice as large as the redshift in the emission would be expected. This is expected due to the fact that in the absorption transition, both the VB and CB energies are involved, while in the case of emission only the CB energy is involved. The energy of the VB and CB are both effected by confinement, while the copper energy level remains the same.

Figure 23C shows the redshift in the emission peak position for Cu^+:InP QDs upon shell growth. The encapsulation experiments with Cu^+:InP show deviation from the encapsulation experiments with undoped InP (Figure 22D) regarding the redshift in the emission peak position. For the first monolayers, involving ZnSe, a similar result is obtained, however, the monolayers with ZnS show deviation. In the experiment with undoped InP, the trend observed for the ZnSe continues for the ZnS, indicating Type I½ heterostructured QDs, while for the Cu^+:InP this trend does not continue. The lack of redshift for the ZnS monolayers indicates Type I behaviour. Upon creating a Type I structure, the effective core does not change, therefore, a redshift is not expected for these systems. There are two possible explanations why the InP and the Cu^+:InP differ in behaviour.

The first possibility could be experimental deviation, where in the undoped InP QDs an alloy of the shell, $ZnSe_{1-x}S_x$, is formed, while for the Cu^+:InP, a ZnSe/$ZnSe_{1-x}S_x$/ZnS shell is formed. The $ZnSe_{1-x}S_x$ creates the Type I½ and the ZnSe/$ZnSe_{1-x}S_x$/ZnS creates a Type I.

The other explanation could be that both are Type I½ systems, in which the excited electron is confined in the core/ZnSe and the hole can be delocalized over the entire core/ZnSe/$ZnSe_{1-x}S_x$/ZnS. In this possibility, the redshift trend (for the ZnS) can continue for the InP core, but not for the Cu^+:InP, because the hole gets trapped (Figure 24).

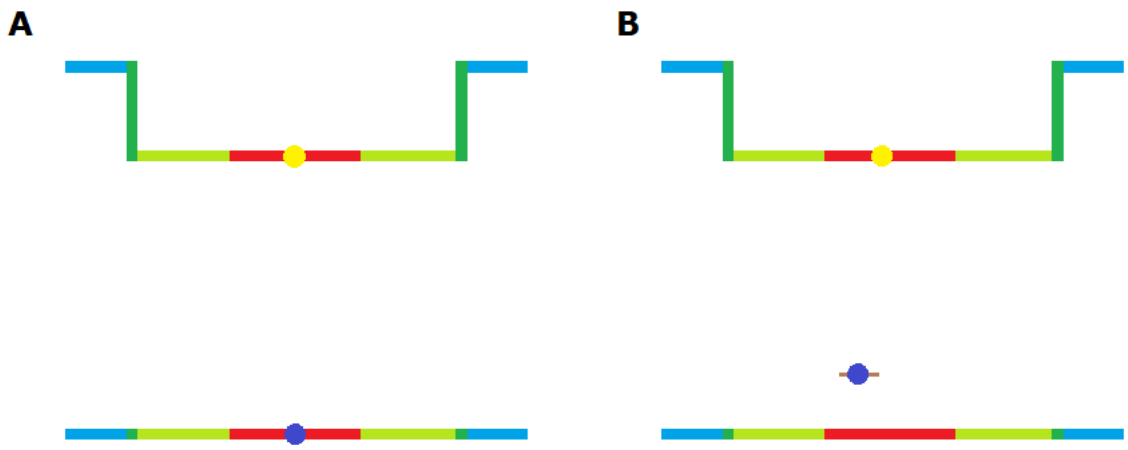

Figure 24: These images depict a possibility for Type I behaviour in a Type I½ QD for the Cu^+ sample mentioned above. The red lines represent the VB and CB of the InP core, while the light green, green, and blue lines represent the ZnSe, $ZnSe_{1-x}S_x$, and ZnS, respectively. The brown line is the copper level, and the dark blue and yellow dots are the hole and excited electron, respectively. A) This image shows the undoped sample, where the hole is penetrates the entire shell, and the electron is confined into the core and the ZnSe part of the shell. B) This image shows the same for the electron but the core is localised at the Cu^+.

In order to get more insight in this system, more experiments shall have to be performed. By varying the thickness of the ZnS sub shell, more information can be gained on the type of heterostructured QD this system is.

Figure 24D shows the FWHM of the emission of the doped QDs, which shows similar behaviour as the FWHM of the undoped QDs. However, the drop in FWHM is only ±15 meV instead of the ±30 meV observed in the undoped QDs, which is likely due to the fact that the emission of the Cu^+ doped QDs is only effected by Gaussian on the energy level of the CB, instead of the Gaussians on both the VB and CB (undoped QDs). The fact that the FWHM rises for the 6^{th} and 7^{th} monolayers is probably because the emission is at the edge of the detectors capability, which gives noise in the spectra and this is difficult to fit properly.

4.3 Variation in the copper dopant

In this section, the effects of the copper dopant concentration are explored. During the doping of the InP QDs, copper(II) stearate of a certain concentration was added to the reaction mixture. This concentration was varied during these experiments. After the post-synthesis doping, the QDs were encapsulated in a 3 monolayer shell. The samples with different Cu^+ dopant concentrations are characterized using ICP, absorption and emission spectroscopy, and time resolved emission spectroscopy.

4.3.1 ICP data

During the copper dopant concentration variation experiments, different concentration of $Cu(st)_2$ were added to the reaction mixture, creating various concentrations of $Cu(st)_2$ in the reaction mixture and these Cu^+ concentrations are measured using ICP. Similar to previous experiments, batches of InP are split into 4, 3 of which are used for doping, while 1 is used for undoped reference. Figure 25 shows the Cu^+/In^{3+} ratio as function of this $Cu(st)_2$ concentration in the reaction mixture and each batch of InP is represented with a different colour.

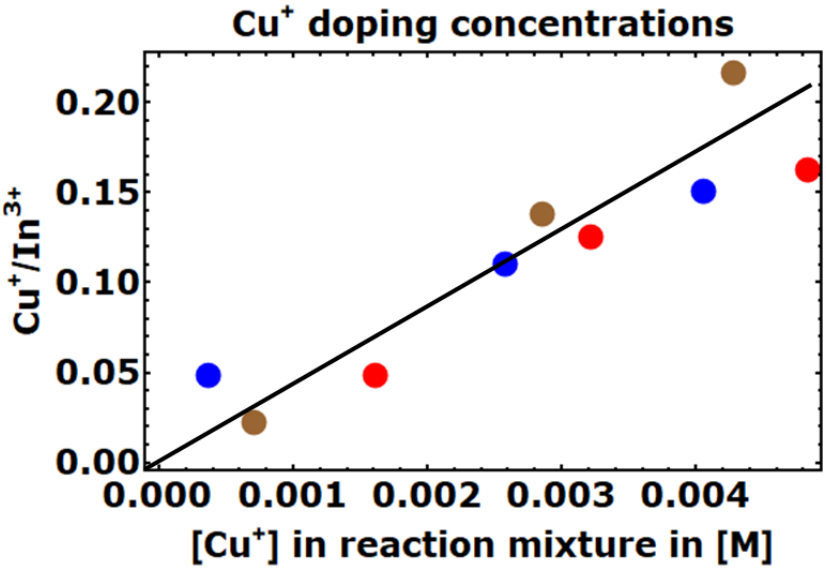

Figure 25: This graph depicts the Cu^+/In^{3+} ratio as function of the copper concentration during the doping phase. The colour of the data points indicates which cores originated from the same batch. The blackline is a guide to the eye and appears somewhat linear within the measured range.

Figure 25 shows that the Cu^+/In^{3+} increases as the copper concentration in the reaction mixture increases. The blue and brown batch hint at a linear relation between the Cu^+/In^{3+} ratio and the copper in the reaction mixture, while the red batch does not hint at a linear relation. The slope of the ratio as function of the copper concentration in the reaction mixture is different for each batch, most likely depending on several factors, such as core shape and size, and surface chemistry.

4.3.2 Absorption and emission data

Figure 26A shows the absorption spectra from four different batches of InP cores (purple, green, brown, and red). Each of these batches show absorption spectra for different copper concentrations. The lighter shades of the colours represents the lowest copper concentration, while the darker shades represent the higher doped samples and all spectra are normalized at 400 nm. The peak seems to decrease in intensity and broaden at higher copper dopant concentrations. The tail of the absorption increases at higher copper concentrations as well, which is most clearly visible in the green batch. *Xie et al.* observed this behaviour as well. [22]

Figure 26B shows the absorption spectra of various doped samples with different dopant concentrations, as well as the absorption spectrum of an undoped sample. All the samples in this image are from the same batch core particles and both doped and undoped have the same shell grown around them.

Figure 26: (A) This graph shows the absorption spectra for samples with several different copper concentrations. Each batch of core particles has its own colour and lighter shades of the colour have lower dopant concentrations than the darker shader. Note that the intensity decreases upon high levels of doping and the peak broadens as well.

There are several explanations possible for the decrease in peak intensity and the increase of the FWHM of the absorption peaks.

- Distortion of oscillation strength of the InP unit cell, due to the interstitial copper dopants
- Absorption of a photon by a Cu^{+} ion
- Damage to cores due to the unknown reduction reaction of Cu^{2+} to Cu^{+} during the doping phase

The peak broadening is stronger for samples with higher dopant concentrations, which can be explained by all three possibilities. It can be explained by the distortion in the oscillation strength, because higher copper dopant concentrations lead to more distortions within the InP unit cells and will, therefore, effectively broaden the absorption peaks. The absorption of photons by Cu^{+} ($ML_{CB}CT$ process) explain this, because higher copper concentrations means more absorption by Cu^{+}, which causes the tail to increase significantly. Therefore, the S transition peak appears broader. Also the charge change of the Cu^{+} to Cu^{2+} will affect the unit cells, due to coulomb interactions. Lastly, the broadening could be explained due to the unknown reduction reaction of Cu^{2+} to Cu^{+} in the doping phase. Cu^{2+} ions are reduced to Cu^{+} by an unknown reaction, which could cause damage if the InP lattice is involved in the reaction. Higher concentrations of Cu^{2+} would mean that there is more potential damage, which could broaden the peak. However, this reason is less likely, because it is expected that the reduction is performed outside of the lattice by electron rich ligands and solvents. Therefore, the decrease in intensity and the broadening of the peak are likely due to a combination of the distortions in the oscillation strength in the InP unit cells and the $ML_{CB}CT$ absorption process.

From emission spectra, the maximum emission intensity is determined for QDs with various Cu^+ dopant concentrations. Figure 27 shows these maximum intensities as function of the concentration copper ions in the reaction mixture. 4 different batches of InP core particles were used for this experiment and each batch of InP cores was split for three different copper concentrations. All the QDs have a shell of 3 monolayers of shell material.

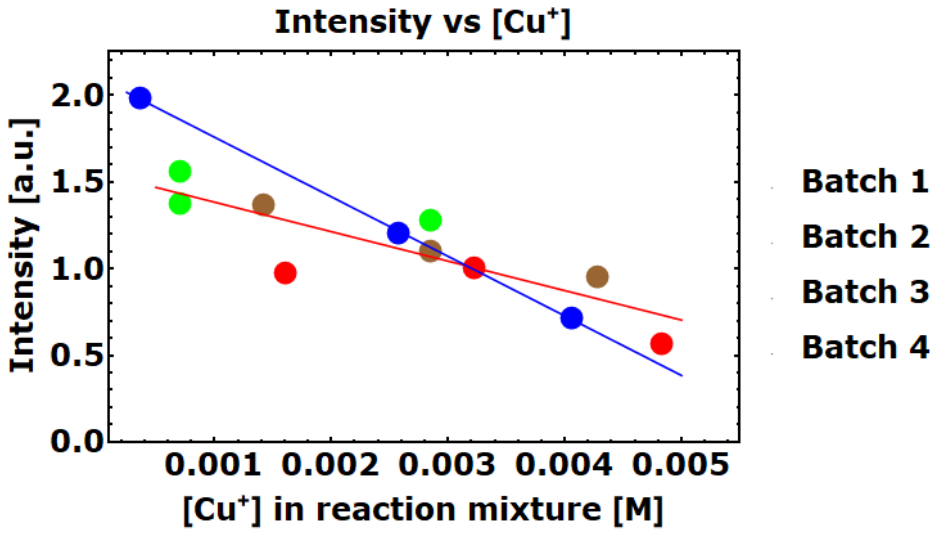

Figure 27: This graph depicts the max intensity of the emission as fuction of the copper concentration in the reaction mixture. Each batch of InP core particles is represented with a diferent colour. The emission was measered utilizing a CCD, a 400 nm longpass filter and a 395 nm LED (excitation source). The emission is corrected utilizing the absorption at 395 nm (excitation wavelength).

From Figure 27, it is clear that lower concentrations of copper yield higher photoluminescence. This seems to be in contrast with the results as presented for CdSe QDs in Figure 14. However, it should be noted that the range of doping concentration is completely different for both studies. *Tananaev et al.* used a doping range of 0 to 0.5% [45], while in this research the doping range encompasses 2% to 22%. This gives rise to two different possibilities:

- The system of Cu^+:CdSe is fundamentally very different from Cu^+:InP.
- There is a non-radiative exciton decay pathway present at higher dopant concentrations.

It is possible that there is a difference between Cu^+:InP and Cu^+:CdSe, because they have different crystal stuctures, zinc blende and wurtzite respectively. Also the InP and CdSe are III-V and II-VI systems, respectively. However, *Knowles et al.* show that Cu^+:InP, Cu^+:CdSe and $CuInS_2$ have similar trends in their optical properties. [20] The materials all show broad emission bands and large effective stokes shifts. They all three show the same magnetic-exchange and zero field splitting between singlet and triplet states. It is concluded that their excited-states are indistinguishable. Therefore, it is unlikely that the difference in host lattice causes an opposite trend for photoluminescence as function of doping material.

The second explanation comes from the difference in doping concentrations. Higher dopant concentrations may introduce an extra non-radiative decay pathway. An increase in Cu^+ could cause an increase in distortions in the InP lattice, which might lead to several defects. These defects can facilitate non-radiative decay. Another explanation could be that the increase in Cu^+ concentration allows for charge-transfer interactions. The energy of a recombined exciton (1.4-1.5 eV) could be transferred to two holes on $Cu^{(2)+}$ ions (600 meV per trapped hole) nearby, allowing de-trapping of the holes and thus facilitating non-radiative decay. However, two excitons within the same QD are needed for this charge transfer process.

To make the trend more clear, a guide for the eye is drawn in Figure 27. Note that there are two lines present. The red line is the trend visible for batch 1, 2, and 3, while the blue line is for batch 4. A separate line is drawn for batch 4, because it appears to deviate from the other samples. Batch 4 QDs are synthesised with another indium precursor, which can result in different qualities of InP cores (e.g. size, internal defects, and surface composition) and doping environment.

QY measurements where performed for the sample with the with the lowest copper concentration. The sample was doped using 0.001M of $Cu(st)_2$ during the doping phase and had 3 monolayers of shell material. The measurements resulted in a 21% QY (see Figure 35 in appendix 3).

4.3.3 Lifetime analyses

The top graph in Figure 28 shows the decay curves for samples with different values of copper dopant concentration. The light blue spectrum represents the decay curve for undoped encapsulated InP QDs, while the purple, green and red spectra represent the decay curves for samples in which 0.001M, 0.007M, and 0.011M $Cu(st)_2$ was added during the doping phase, respectively. Note that the decay curve of the undoped QDs decays much faster (± one order of magenitude) than the copper-doped QDs. The spectra of the doped QDs are very similar to each other when compared to the undoped spectra. The decay seems to be slightly faster for higher copper concentrations.

The bottom graph of Figure 28 shows the decay curves with different excitation wavelengths for the 0.001M sample. The wavelengths utilized for this experiment are 375, 510, and 656 nm. It appears that all three excitation wavelengths give almost exactly the same curve.

Table 2 gives the lifetimes according to the fits shown in Figure 28. The undoped spectrum is fitted with a mono-exponential decay and a power-law, in which P is the chance of carrier separation and α is a power exponent. [61] The doped spectra are fitted with a bi-exponential curve.

Table 2: Lifetimes of QDs with various dopant concentrations

[Cu] added during doping	τ_1	τ_2
0M	41.3 ns	Powerlaw with P=15% and α=2.1
0.001M	0.315 µs	0.746 µs
0.007M	0.236 µs	0.634 µs
0.011M	0.232 µs	0.610 µs

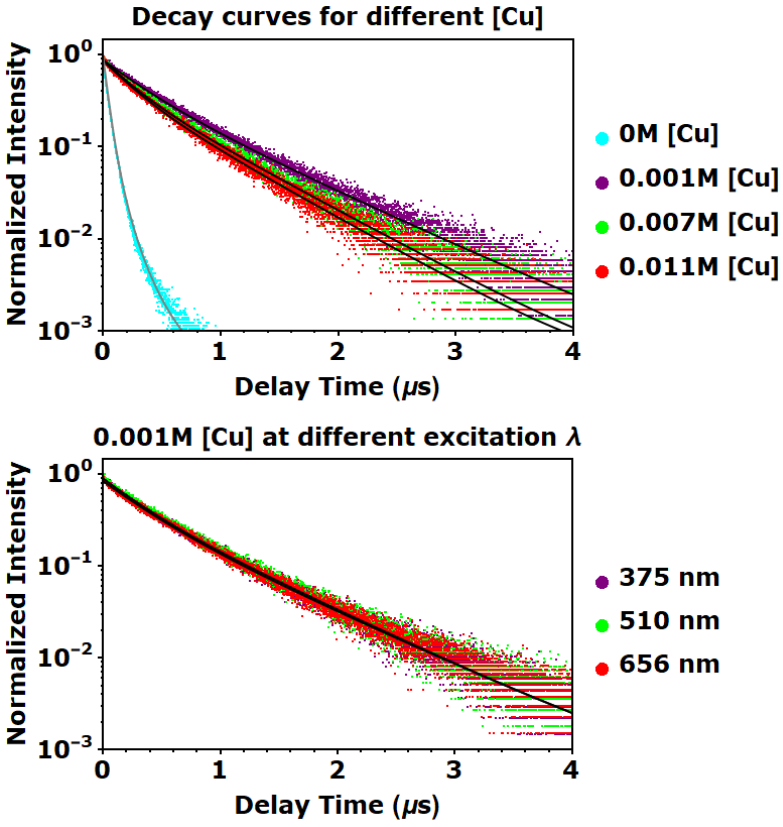

Figure 28: These graphs depict lifetime measurements. Top: This graph shows the decay curves for samples with several different copper concentrations. The samples were excited at 510 nm with 10 µs pulses. Bottom: this graph shows that the lifetime in these samples is more or less the same for all excitation wavelengths. The sample was excited with 375, 510, and 656 nm with 10 µs pulses.

As table 2 and Figure 28 show that, the lifetime of undoped QDs is much faster than the lifetime of the doped QDs. The lifetime of 41.3 ns for undoped QDs is similar to values found in literature. For example, InP/ZnS has a lifetime of 36.7 ns. [62] The longer values for the doped InP QDs are expected as well. *Knowles et al.* found high values of several hundreds of nanoseconds [20], which is observed in this research as well.

The slight decrease in lifetime upon increasing the copper dopant concentration is expected. The only variable in the experiment is the copper concentration of the solution added during doping. This allows for higher doping concentrations, as seen in the ICP data, which allows for more diffusion towards the middle of the QD. In the middle of the particle, the wave function overlap between excited electrons and trapped holes will be larger. Therefore, the decay of the exciton will be faster.

An additional consequence of the high copper concentration could be hopping of trapped holes from $Cu^{(2)+}$ to Cu^{+}, resulting in more holes near the centre of the QD, which shortens the lifetime. This hopping is less likely, because direct hopping from $Cu^{(2)+}$ to Cu^{+} needs to occur. For this, higher concentrations may be necessary. The hopping would need to occur directly, because de-trapping of the holes to the VB takes 600 meV. This is more energy than is available from thermal- or phononic energy.

The wavelengths in the bottom graph of Figure 28 (375 nm, 510 nm, and 656 nm) were chosen, because they excite electrons in the shell, core, and doping ions, respectively. The bottom of Figure 28 shows that exciting electrons in these different components of the QDs yield indistinguishable decay curves. This means that the decay mechanism is independent of the excited wavelength.

4.4 Transient absorption spectroscopy measurements

During the research for this thesis, a set of samples were synthesised for the purpose of TA measurements, which are performed in order to gain insight in the decay mechanisms of the excited electrons. The result of a Cu^{+}:InP/$ZnSe_{1-x}S_x$ TA measurement is depicted in Figure 29. Figure 29A shows a graph containing the full information of the TA measurement with the wavelength on the x-axis, the delay time on the y-axis, and the absorption bleach in colour. In this graph, blue is a strong bleach and white is a weak positive absorption. Figure 29B show the horizontal cross-sections visible in Figure 29A, and shows the bleach as function of the wavelengths at 2 points in time. Note that the peak at ~480 nm disappears over time and that the peak at ~575 nm appears over time. Figure 29C shows the vertical cross-sections indicated in Figure 29A, and shows the absorption as function of time at two wavelengths.

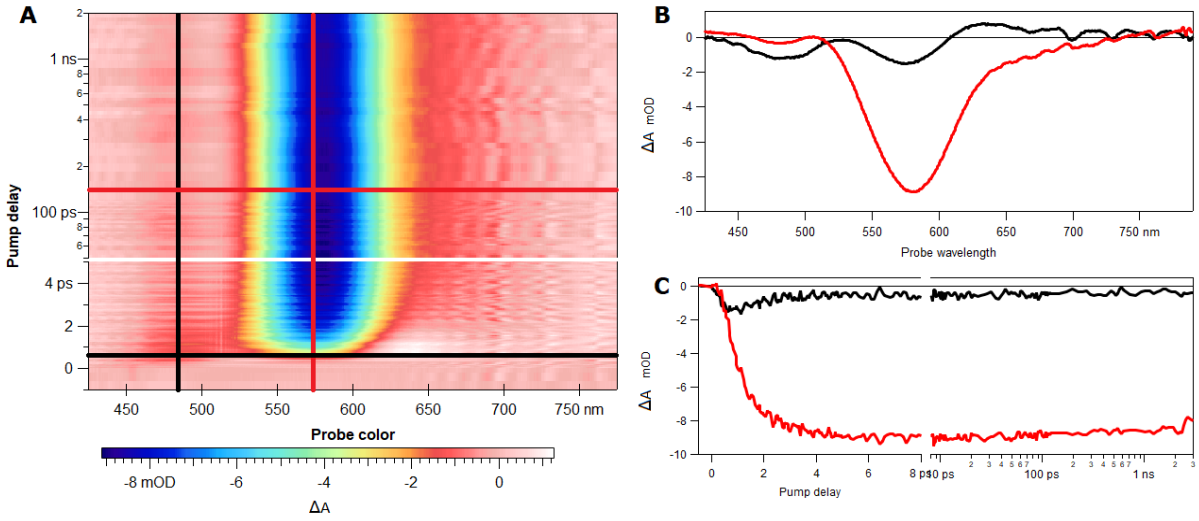

Figure 29: A) This graph shows the complete transient absorption data with time on the y-axis and wavelength on the x-axis. B) This graph shows the red and black horizontal cross-sections in (A). C) This graph shows the red and black vertical cross-sections in (A).

The peak at 480 nm in Figure 29A&B is the absorption bleach from the P transition and the peak at 575 nm is the absorption bleach of the S transition state.

The black line in Figure 29B, at t = 1 ps, shows a bleach at 480 nm, while the peak at 575 nm shows a small bleach (compared to bleach of the red line at 575 nm). The bleach at 480 nm means that absorption does occur in lesser amounts in the excited state (at this specific wavelength), which means that the P state is at least partially populated. The fact that the bleach at 580 ns is small indicates that absorption does occur, which means that the S excited state is mostly unoccupied.

At the redline (t = 150 ps), the bleach at 480 nm becomes almost 0 and the bleach 575 nm is increased, which indicates that the excited electrons in the P state have relaxed into the S state, allowing P transition absorption and blocking S transition absorption. This is shown in Figure 29C, where the it is shown that the absorption of the S transitions (red) starts to grown as the absorption of the P transition (black) starts to decrease. It should be noted that near t = 1 ps, the absorption values are not completely correct, which is due to the time resolution at which the device can measure, and due to the system response time of the device. At t = 0 ps the value of the black line (P transition) should be 1/3 of the biggest value of the red line (S transition), because the ratio of degeneracy of S orbital/P orbital is 1/3 (2/6).

The small white spot (weak positive absorption) near 640 nm at t ≈ 1 ps is due to a small redshift in the excited S state. This redshift is due to coulomb interactions between the electrons in the occupied excited P state and the empty excited S state, pushing the energy of this state down in energy when an electron is excited to this state. The redshift of this energy level, results in a slight positive bleach upon subtracting the original absorption spectrum.

Figure 29C shows that the black line (at 480 nm) does not become completely 0 and a small bleach remains, which is also the result of coulombic interactions. After the electrons have relaxed from the 1P excited state to the 1S excited state, the P state becomes available again for absorption, which should result in the complete disappearance of the bleach. However, this absorption is shifted due to coulombic interaction with the electron in the 1 S excited state, resulting in a false bleach in Figure 29.

The red line Figure 29C does not return to 0 in this graph because the lifetime of the exciton is several hundred nanoseconds, which is far outside the measured range.

5 Conclusion

In summary, the desired Cu^+:InP/$ZnSe_{1-x}S_x$ QDs were synthesized utilizing a hot-injection synthesis with indium(III) myristate and $P(TMS)_3$ as indium and phosphor precursor, respectively. This was followed by the post-synthesis doping method, utilizing $Cu(st)_2$. Finally, the shell was grown utilizing SILAR with $Zn(st)_2$, TOP-Se, and TOP-S as precursors. During the hot-injection synthesis of InP QDs, size focussing and growth according to the cube root of time are observed, which are attributed to the digestive ripening growth mechanism. A 600 meV down-shift in emission is observed for Cu^+:InP and Cu^+:InP/$ZnSe_{1-x}S_x$ compared to InP/$ZnSe_{1-x}S_x$, which is due to the $ML_{CB}CT$ excited state. This reduces the overlap between absorption and emission from ±60% to ±10%, which should result in a decreased reabsorption in LSCs. Long lifetimes associated with copper doped QDs are observed.

Optimization experiments for shell thickness and copper dopant concentration were performed. Experiments show that the quantum yield increases with increasing shell thickness and decreasing copper dopant concentration. The highest QY measured for the shell optimization, which utilized a standard dopant concentration, was 26%. This was measured for the sample with 7 monolayers. The QY measured for the most luminescent sample of the dopant optimization experiment, which all utilized 3 monolayer shells, was 21%. This was measured for the sample which had 1.25 ml of 0.001 M $Cu(st)_2$ in ODE added during the doping phase. The Cu^+:In^{3+} ratio researched during the dopant optimization experiments ranged from 0.022 to 0.16 according to ICP measurements. According to time resolved emission spectroscopy, lifetime decreases upon an increase of dopant concentration.

TA measurements show that first the 1P excited state is populated. Over time, the bleach at the P transition decreases, while the bleach of the S transition increases, which means that the electron occupying 1P excited state relax into the 1S excited state. This process occurs over several pico-seconds. The recombination of the exciton is not observed, because the lifetime of the exciton is far out of the measured range.

6 Outlook

It seems that Cu^+:InP/$ZnSe_{1-x}S_x$ is a good potential choice for luminescent material in LSCs. However, there are still aspects to be researched for this system. Due to time constrains it was not possible to combine the insight gained from the shell- and dopant variation. The QY of the best possible sample within the range of the experiments can be estimated by using the known QYs, and Figure 27 and Figure 33 (Appendix 3). This is possible by two methods.

First method: it was observed that samples with standard copper dopant concentration and 7 monolayers of shell have a QY of 26%. According to Figure 27, the luminescence of QDs with standard Cu^+ doping can increased with a factor 2 by going to lower Cu^+ concentrations, which would give a QY of 52%. Second method: The sample with low Cu^+ dopant concentration and 3 monolayers of shell has a QY of 21%. According to Figure 33, the luminescence of QDs with 3 monolayers of shell can be increased with a factor 2 by growing a 7 monolayer shell, which would give a QY of 42%. Therefore, the estimated QY for QDs with low Cu^+ concentration and 7 monolayer shells would be in the range of 40-50%, depending on core and shell quality.

Improvement in QY is achievable by further optimization of both encapsulation and the doping departments. In addition, further research on the optical properties and the effect of the copper dopant concentration upon the optical properties are important to gain a better understanding in these systems. Therefore, I propose a list of possible and relevant future experiments in order to improve the QY and/or to understand these systems better:

- Improving the QY of Cu^+:InP/$ZnSe_{1-x}S_x$:
    - Encapsulation experiments.
        - Growing thicker shells than the current 7 monolayers.
        - Using different ratios of the sub shells of the current encapsulation system.
            - Experiments show that the QY increases the most upon the deposition of ZnSe. Increasing the ZnSe portion of the $ZnSe_{1-x}S_x$ system might increase the QY further.
            - Theory states that Type I semiconductor hetero nanocrystals should have larger QY. The ZnS should realize this in the $ZnSe_{1-x}S_x$ system, however, the ZnS might be too thin and the electron will tunnel into the ZnS anyway. Therefore, increasing the ZnS portion of the $ZnSe_{1-x}S_x$ system might increase the QY.
        - Growing thick shells by methods other than SILAR. The SILAR shell is grown monolayer for monolayer. This means that the particle is exposed to high heat for prolonged amounts of time. This could affect the quality of the core. Therefore, faster encapsulation synthesis might be preferential.
    - Dopant experiments.
        - Research a different range of Cu^+ doping. The results in this thesis show that lower copper concentrations have higher luminescence. Exploration of a copper dopant concentration range of 0.1-5% is necessary.
        - Other doping methods might increase the QY.
- Analyses to be performed on Cu^+:InP/$ZnSe_{1-x}S_x$ to gain more information on the system:
    - Transient absorption spectroscopy can be utilized to learn more about the hole trapping and the cooling of the hot-electron.
    - Cyclic voltammetry can be utilized to obtain more insight in the energy level of dopant in the host lattice.
    - Temperature-dependent absorption and emission, which gives information on temperature dependence of the broadening observed in the Cu^+-doped QDs.
- Similar systems to be researched:

- $ZnSe/Cu^{+}:InP/ZnSe_{1-x}S_x$ is a potential material to explore. Encapsulating monodisperse ZnSe in InP may give more control over the uniformity of the InP. This might improve the luminescent properties of the InP. This system would make the InP a Type I infinite quantum well and may give rise to interesting properties.
- Cu^{+}:In(Zn)P is another possibility for a new material. In(Zn)P QDs has proven to have higher QY than InP QDs. Therefore, it might be interesting for the LSC application.

7 Acknowledgements

Under the supervision of Daniël Vanmaekelbergh, my first examiner, and Tim Prins, my daily supervisor, I conducted research on the synthesis and characterization of Cu^{+}:InP/$ZnSe_{1-x}S_x$ for luminescent solar concentrators. Upon completing this thesis, I can conclude that I have learned a lot over the past year. Not just in knowledge about the systems in this thesis, but about other research and research in general as well. Therefore, I would like to thank Daniël Vanmaekelbergh and Tim Prins for granting me the opportunity to conduct this research at Condensed Matter and Interfaces. Apart from providing me with the opportunity, I would also like to thank them for their supervision, help, guidance, and above all patience. I would like to thank Celso de Mello Donega as second examiner.

Further, I would like to thank Elleke van Harten for sharing her knowledge on the synthesis of InP QDs and everybody else who helped me improve my theoretical, practical, and technical assistance. Finally, I would like to thank all the students, PhD candidates, post-doctorates, and staff members for the great experience at CMI. Lunches and the first Friday of the month borrels were always fun.

8 References

[1] Antartic Climate & Ecosystems Cooperative Research Centre, “Position Analysis: Climate Change, Sea-Level Rise and Extreme Events: Impacts and Adaptation Issues,” Hobart, 2008.

[2] D. J. Wuebbles and A. K. Jain, “Concerns about climate change and the role of fossil fuel use,” *Fuel Processing Technology,* vol. 71, pp. 99-119, 2001.

[3] M. S. Dresselhaus and I. L. Thomas, “Alternative energy technologies,” *Nature,* vol. 414, pp. 332-337, 2001.

[4] N. Kannan and D. Vakeesan, “Solar energy for future world: - A review,” *Renewable and Sustainable Energy Reviews,* vol. 62, p. 1092–1105, 2016.

[5] “Zero-energy building,” Wikipedia, 15 03 2018. [Online]. Available: https://en.wikipedia.org/wiki/Zero-energy_building. [Accessed 17 03 2018].

[6] “What are the most efficient solar panels on the market?,” Energysage, [Online]. Available: https://news.energysage.com/what-are-the-most-efficient-solar-panels-on-the-market/. [Accessed 16 03 2018].

[7] C.-C. Chen, L. Dou, C.-h. Chung, T.-B. Song, Y. B. Zheng, S. Hawks, G. Li, P. S. Weiss and Y. Yang, “Visibly Transparent Polymer Solar Cells Produced by Solution Processing,” *ACS Nano,* vol. 6, no. 8, pp. 7185-7190, 2012.

[8] H. Hernandez-Noyola, D. H. Potterveld, R. J. Holt and S. B. Darling, “Optimizing luminescent solar concentrator design,” *Energy & Environ.l Sci.,* vol. 5, pp. 5798-5802, 2012.

[9] M. G. Debije and P. P. C. Verbunt, “Thirty years of luminescent solar concentrator research: solar energy for the built environment,” *Adv. Energy Mater.,* vol. 2, pp. 12-35, 2012.

[10] M. J. Currie, J. K. Mapel, T. D. Heidel, S. Goffri and M. A. Baldo, “High-Efficiency Organic Solar Concentrators for Photovoltaics,” *Science,* vol. 321, pp. 226-228, 2008.

[11] W. G. J. H. M. van Sark, K. W. J. Barnham, L. H. Slooff, A. J. Chatten, A. Büchtemann, A. Meyer, S. J. McCormack, R. Koole, D. J. Farrel, R. Bose, E. E. Bende, A. R. Burgers, T. Budel, J. Quilitz, M. Kennedy, T. Meyer, D. Vanmaekelbergh, A. Meijerink and C. De Mello Donega, “Luminescent Solar Concentrators – A review of recent results,” *Opt. Express,* vol. 16, no. 26, p. 20, 2008.

[12] L. H. Slooff, E. E. Bende, A. R. Burgers, T. Budel, M. Pravettoni, R. P. Kenny, E. D. Dunlop and A. Büchtemann, “A luminescent solar concentrator with 7.1% power conversion efficiency,” *Phys. Stat. Sol. (RRL),* vol. 2, no. 6, p. 257–259, 2008.

[13] H. Li, K. Wu, J. Lim, H.-J. Song and V. I. Klimov, “Doctor-blade deposition of quantum dots onto standard window glass for low-loss large-area luminescent solar concentrators,” *Nature Energy,* vol. 1, p. 9, 2016.

[14] N. D. Bronstein, Y. Yao, L. Xu, E. O'Brien, A. S. Powers, V. E. Ferry, P. A. Alivisatos and R. G. Nuzzo, "Quantum Dot Luminescent Concentrator Cavity Exhibiting 30-fold Concentration," *ACS Photonics,* vol. 2, p. 1576−1583, 2015.

[15] C. S. Erickson, L. R. Bradshaw, S. McDowall, J. D. Gilbertson, D. R. Gamelin and D. L. Patrick, "Zero-ReabsorptionDoped-Nanocrystal Luminescent Solar Concentrators," *ACS Nano,* vol. 8, no. 4, p. 3461–3467, 2014.

[16] I. Coropceanu and M. G. Bawendi, "Core/Shell Quantum Dot Based Luminescent Solar Concentrators with Reduced Reabsorption and Enhanced Efficiency," *Nano Lett.,* vol. 14, p. 4097−4101, 2014.

[17] Z. Krumur, S. J. Pera, R. J. A. van Dijk-Moes, Y. Zhao, A. F. P. de Brouwer, E. Groeneveld, W. G. J. H. M. van Sark, R. E. I. Schropp and C. De Mello Donega, "Tackling self-absorption in luminescent solar concentrators with type-II colloidal quantum dots," *Solar Energy Materials & Solar Cells,* vol. 111, pp. 57-65, 2013.

[18] L. R. Bradshaw, K. E. Knowles, S. McDowall and D. R. Gamelin, "Nanocrystals for Luminescent Solar Concentrators," *Nano Lett.,* vol. 15, p. 1315−1323, 2015.

[19] F. Meinardi, A. Colombo, K. A. Velizhanin, R. Simonutti, M. Lorenzon, L. Beverina, R. Viswhanatha, V. I. Klimov and S. Brovelli, "Large-area luminescent solar concentrators based on 'Stokes-shift-engineered' nanocrystals in a mass-polymerized PMMA matrix," *Nature Photonics,* vol. 8, pp. 392-399, 2014.

[20] K. E. Knowles, H. D. Nelson, T. B. Kilburn and D. R. Gamelin, "Singlet−Triplet Splittings in the Luminescent Excited States of Colloidal Cu+:CdSe, Cu+:InP, and CuInS2 Nanocrystals: Charge-Transfer Configurations and Self-Trapped Excitons," *JACS,* vol. 137, pp. 13138-13147, 2015.

[21] K. Nose, T. Omata and S. Otsuka-Yao-Matsuo, "Colloidal Synthesis of Ternary Copper Indium Diselenide Quantum Dots and Their Optical Properties," *J. Phys. Chem.,* vol. 113, pp. 3455-3460, 2009.

[22] R. Xie and X. Peng, "Synthesis of Cu-Doped InP Nanocrystals (d-dots) with ZnSe Diffusion Barrier as Efficient and Color-Tunable NIR Emitters," *JACS,* vol. 131, no. 30, pp. 10645-10651, 2009.

[23] M. Debije, "Renewable energy: Better luminescent solar panels in prospect," *Nature,* vol. 519, pp. 298-29, 2015.

[24] L. M. Chávez, "Optimization of a Luminescent Solar Concentrator," Delft University of Technology, Delft, 2017.

[25] S. M. El-Bashir, O. A. AlHarby and M. S. AlSalhi, "Thin-Film LSCs Based on PMMA Nanohybrid Coatings: Device Optimization and Outdoor Performance," *International Journal of Photoenergy,* vol. 2013, p. 10 pages, 2013.

[26] C. Yang and R. R. Lunt, "Limits of Visibly Transparent Luminescent Solar," *Advanced Optical Materials,* vol. 5, p. 10, 2017.

[27] C. B. Murray, D. J. Norris and M. G. Bawendi, “Synthesis and characterization of nearly monodisperse CdE (E = sulfur, selenium, tellurium) semiconductor nanocrystallites,” *JACS,* vol. 115, no. 19, p. 8706–8715, 1993.

[28] F. T. Rabouw and C. De Mello Donega, “Excited-State Dynamics in Colloidal Semiconductor Nanocrystals,” *Top. Curr. Chem.,* vol. 374, p. 30, 2016.

[29] D. Bera, Q. Lei, T.-K. Tseng and P. H. Holloway, “Quantum Dots and Their Multimodal Applications: A Review,” *Materials,* vol. 3, pp. 2260-2345, 2010.

[30] C. De Mello Donega, Nanoparticles Workhorses of the Nanoscience, Utrecht: Springer, 2014.

[31] D. Mocatta, Cohen Guy, J. Schattner, O. Millo, E. Rabani and U. Banin, “Heavily Doped Semiconductor Nanocrystal Quantum Dots,” *Science,* vol. 332, pp. 77-81, 2011.

[32] W.-H. Chang, T. M. Hsu, N.-T. Yeh and J.-I. Chyi, “Carrier Transfer Effects and Thermal Activation Behaviors in the Photoluminescence of In(Ga)As Self-assembled Quantum Dots,” *CHINESE JOURNAL OF PHYSICS,* vol. 40, no. 5, pp. 548-559, 2002.

[33] C. De Mello Donega, “Synthesis and properties of colloidal heteronanocrystals,” *Chem. Soc. Rev.,* no. 40, pp. 1512-1546, 2011.

[34] S. Kim, T. Kim, M. Kang, S. K. Kwak, T. W. Yoo, L. S. Park, I. Yang, S. Hwang, J. E. Lee, S. K. Kim and S.-W. Kim, “Highly Luminescent InP/GaP/ZnS Nanocrystals and Their Application,” *JACS,* vol. 134, pp. 3804-3809, 2012.

[35] S. G. Kwon and T. Hyeon, “Formation Mechanisms of Uniform Nanocrystals via Hot-Injection and Heat-Up Methods,” *Small,* vol. 7, no. 19, pp. 2685-2702, 2011.

[36] J. Lim, W. K. Bea, J. Kwak, S. Lee, C. Lee and K. Char, “Perspective on synthesis, device structures, and printing processes for quantum dot displays,” *Opt. Mater. Express,* vol. 2, no. 5, pp. 594-628, 2012.

[37] A. Baldan, “Review Progress in Ostwald ripening theories and their applications to nickel-base superalloy,” *Journal of Materials Science,* vol. 37, p. 2171– 2202, 2002.

[38] X. M. Lin, G. M. Wang, C. M. Sorensen and K. J. Klabunde, “Formation and Dissolution of Gold Nanocrystal Superlattices in a Colloidal Solution,” *J. Phys. Chem. B,* vol. 103, pp. 5488-5492, 1999.

[39] V. I. Irzhak, “Digestive Ripening of Nanoparticles,” *Russ. J. Phys. Chem.,* vol. 91, no. 8, pp. 1502-1506, 2017.

[40] J. R. Shimpi, D. S. Sidhaye and B. L. V. Prasad, “Digestive Ripening: A Fine Chemical Machining Process on the Nanoscale,” *Langmuir,* vol. 33, pp. 9491-9507, 2017.

[41] D.-K. Lee, S.-I. Park, J. K. Lee and N.-M. Hwang, “A Theoretical Model for Digestive Ripening,” *Acta Materialia,* vol. 55, pp. 5281-5288, 2007.

[42] B. L. V. Prasad, S. I. Stoeva, C. M. Sorensen and K. J. Klabunde, “Digestive Ripening Agents for Gold Nanoparticles: Alternitives to Thiols,” *Chem. Mater.,* vol. 15, pp. 935-942, 2003.

[43] S. Cingarapy, Z. Yang, C. M. Sorensen and K. J. Klabunde, “Synthesis of CdSe/ZnSe and CdTe/ZnSe Quantum Dots: Refined Digestive Ripening,” *Journal of Nanomaterials,* p. 12, 2012.

[44] K. E. Knowles, K. E. Hartstein, T. B. Kilburn, A. Marchioro, H. D. Nelson, P. J. Whitham and D. R. Gamelin, “Luminescent Colloidal Semiconductor Nanocrystals Containing Copper: Synthesism Photophysics and Aplications,” *Chem. Rev.,* vol. 116, pp. 10820-10851, 2016.

[45] P. N. Tanananaev, S. G. Dorofeev and T. A. Kuznetsova, “Preparation of Copper-Doped CdSe Nanocrystals,” *Inorg. Mater.,* vol. 45, no. 4, pp. 347-351, 2009.

[46] L. Yang, K. E. Knowles, A. Gopalan, K. E. Hughes, M. C. James and D. R. Gamelin, “Synthesis of Monodisperse Colloidal Copper-Doped CdSe Nanocrystals Mediated by Ligand-Copper Interactions.,” *Chem. Mater.,* vol. 28, pp. 7375-7384, 2016.

[47] J. Ministro, “A study on the synthesis and the optical properties of InP-based quantum dots,” University Gent, Gent, 2014.

[48] P. Mushonga, M. O. Onani, A. M. Madiehe and M. Meyer, “Indium Phosphide-Based Semiconductor Nanocrystals and Their Applications,” *Journal of Nanomaterials,* vol. 2012, p. 11, 2012.

[49] D. Battaglia and X. Peng, “Formation of High Quality InP and InAs Nanocrystals in a Noncoordinating Solvent,” *Nano Lett.,* vol. 2, no. 9, pp. 1027-1030, 2002.

[50] D. C. Gary, B. A. Glassy and B. M. Cossairt, “Investigation of Indium Phosphide Quantum Dot Nucleation and Growth Utilizing Triarylsilylphosphine Precursors,” *Chem. Mater.,* vol. 26, pp. 1734-1744, 2014.

[51] P. M. Allen, B. J. Walker and M. G. Bawendi, “Mechanistic insight into the formation of InP quantum dots,” *Angew. Chem. Int. Ed. Engl.,* vol. 49, no. 4, pp. 760-762, 2010.

[52] D. C. Gary, T. W. Maxwell, S. J. L. Billinge and B. M. Cossairt, “Two-Step Nucleation and Growth of InP Quantum Dots via MagicSized Cluster Intermediates,” *Chem. Mater.,* vol. 27, pp. 1432-1441, 2015.

[53] D. K. Harris and M. G. Bawendi, “Improved Precursor Chemistry for the Synthesis of III-V Quantum Dots,” *JACS,* vol. 134, pp. 20211-20213, 2012.

[54] D. Chen, R. Viswanatha, G. L. Ong, R. Xie, M. Balasubramaninan and X. Peng, “Temperature Dependence of “Elementary Processes” in Doping Semiconductor Nanocrystals,” *JACS,* vol. 131, pp. 9333-9339, 2009.

[55] R. Berera, R. van Grondelle and J. T. M. Kennis, “Ultrafast transient absorption spectroscopy: principles and applications to photosynthetic systems,” *Photosynth. Res.,* vol. 101, pp. 105-118, 2009.

[56] S. Maiti, J. Dana, Y. Jadhav, T. Debnath, S. K. Haram and H. N. Ghosh, “Electrochemical Evaluation of Dopant Energetics and the Modulation of Ultrafast Carrier Dynamics in Cu-Doped CdSe Nanocrystals,” *J. Phys. Chem. C,* vol. 121, pp. 27233-27240, 2017.

[57] K. E. Hughes, K. H. Hartstein and D. R. Gamelin, “Photodoping and Transient Spectroscopies of Copper-Doped CdSe/CdS Nanocrystals,” *ACS Nano,* vol. 12, pp. 718-728, 2018.

[58] P. Ramasamy, N. Kim, Y.-S. Kang, O. Ramirez and J.-S. Lee, “Tunable, Bright, and Narrow-Band Luminescence from Colloidal Indium Phosphide Quantum Dots,” *Chem. Mater.,* vol. 29, p. 6893–6899, 2017.

[59] R.-S. Lui, “Synthesis of InP Quantum Dots and Their Applications,” in *Phosphors, Up Conversion Nano Particles and Their Applications, volume 2*, Taipei, Springer, 2016, p. 473.

[60] S. B. Brichkin, M. G. Spirin, S. A. Tovstun, V. Y. Gak, E. G. Mart’yanova and V. F. Razumov, “Colloidal Quantum Dots InP@ZnS: Inhomogeneous Broadening and Distribution of Luminescence Lifetimes,” *High Energy Chem.,* vol. 50, no. 5, p. 395–399, 2016.

[61] F. T. Rabouw, M. Kamp, R. J. A. van Dijk-Moes, D. R. Gamelin, A. F. Koenderink, A. Meijerink and D. Vanmaekelbergh, “Delayed Exciton Emission and Its Relation to Blinking in CdSe Quantum Dots,” *Nano Lett.,* vol. 15, pp. 7718-7725, 2015.

[62] T. Anoop, P. V. Nair and K. G. Thomas, “InP Quantum Dots: An Environmentally Friendly Material with Resonance Energy Transfer Requisites,” *J. Phys. Chem. C,* vol. 118, p. 3838−3845, 2014.

Appendix 1: List of abbreviations and symbols

Abbreviation	Definition
$[M]_b$	Concentration of monomer in solution
$[M]_r$	Solubility of particle with radius r
0D	0-dimensional
1D	1-dimensional
2D	2-dimensional
3D	3-dimensional
γ	Surface energy
ε	Molar absorptivity
ε_{335}	Absorption coefficient at a wavelength of 335 nm
ε_{410}	Absorption coefficient at a wavelength of 410 nm
Δμ	Extra chemical potential
ΔE_a	Activation energy
ΔG	Gibbs free energy
ΔG_V	Volume free energy per volume
η_{Abs}	Absorption efficiency of the solar spectrum of the luminescent material
η_{Opt}	Optical efficiency
η_{PL}	Luminescent efficiency of the luminescent material
η^*_{PV}	Monochromatic efficiency of the PV cell
η_{RA}	Efficiency of preventing reabsorption
η_{RAP}	Reabsorption probability
η_{Tot}	Total power conversion efficiency
η_{Trap}	Trapping efficiency of photons in the LSC
θ	Azimuth angle
θ_{Crit}	Critical angle
τ	Lifetime
ϕ	In-plane angle
φ_{env}	Envelope function
χ	Root of spherical Bessel function
Ψ_{Bloch}	Bloch wave function
Ψ_{Total}	Wave function for quantum dot
A	Absorption
AM1.5G	Air mass 1.5 global solar flux spectrum
C	Concentration of luminescent material in LSC
CB	Conduction band
CIS	Copper indium sulphide
CISe	Copper indium selenide
d	Diameter
D	Diffusion constant
DAP	Donor-acceptor pair
DOS	Density of states
E_g	Bandgap
eV	Electronvolt

FWHM	Full width at half maximum
$\hbar$	Reduced Planck constant
ICP-OES	Inductively coupled plasma – atomic emission spectroscopy
I_{max}	Maximum intensity
$In(My)_3$	Indium myristate
InP	Indium phosphide
k	Reaction constant
k_b	Boltzmann constant
L	Plate length
$L_{CB}MCT$	Ligand to metal charge transfer
l	Azimuthal quatum number
LSC	Luminescent solar concentrator
MA	Myristic acid
MLCT	Metal to ligand charge transfer
$ML_{CB}CT$	Metal to ligand charge transfer with CB acting as ligand.
N_A	Number of Avogadro
n	Principal quantum number
n_{sub}	Refractive index of waveguide
NIR	Near infra-red
$P(TMS)_3$	Tris(trimethylsilyl) phophine
PV	Photovoltaic
ODE	1-octadecene
QD	Quantum dot
QY	Quantum yield
r	radius
R	Ideal gasconstant
	Reflections
R(r)	Bessel function
r_c	Critical radius
r_{max}	Radius with maximum growth rate
S	Measure of supersaturation
Se	Selenium
SILAR	Successive ionic layer adsorption and reaction
t	Time
t_0	Thickness of the waveguide
T	Temperature
TEM	Transmission electron microscopy
TOP	Trioctylphosphine
TOP-S	Trioctylphosphine-Sulfer complex
TOP-Se	Trioctylphosphine-Selenium complex
UV	Ultra violet
VB	Valance band
V_m	Molar volume
Y_l^m	Function for spherical harmonics
$Zn(st)_2$	Zinc(II)stearate

Appendix 2: Synthesis protocol

The InP synthesis was adapted from *Peng et al.* and was divided into 3 parts. First, the synthesise of InP QDs, followed by the post-synthesis doping with $Cu(st_2)$, and finally, the encapsulation of the Cu^+:InP QDs utilizing SILAR.

InP core synthesis

The InP QD synthesis consisted out of the preparation of the $In(my)_3$ precursor, followed by the actual QD synthesis.

A round-bottom flask with 1.20 mmol, 5.25 mmol myristic acid, and 15 ml ODE was prepared. This mixture was degassed under vacuum on a slenck line, while stirring. After degassing for 30-60 minutes, the solution was heated to 100-120 °C, under vacuum, until the solution became clear. After solution became clear, it was moved into the glovebox.

Inside the glovebox, 5 ml of the previously prepared indium precursor was heated to 188 °C in a three-necked round-bottom flask with vigreux, while vigorously stirring. During the heating of the indium precursor, the phosphor precursor was prepared. 56 µL of $P(TMS)_3$ was added to a mixture of 1 ml TOP, and 370 µL octylamine. Upon reaching 188 °C, the indium precursor was swiftly injected with the phosphor precursor, utilizing a syringe. The temperature was set and kept at 178 °C for 30 minutes before it was quenched with 3 ml of ODE and cooled down by removing the hotplate. Upon completion of the reaction the batch was split in four, for doping and/or encapsulation experiments. Figure 30 gives a scheme of the reaction.

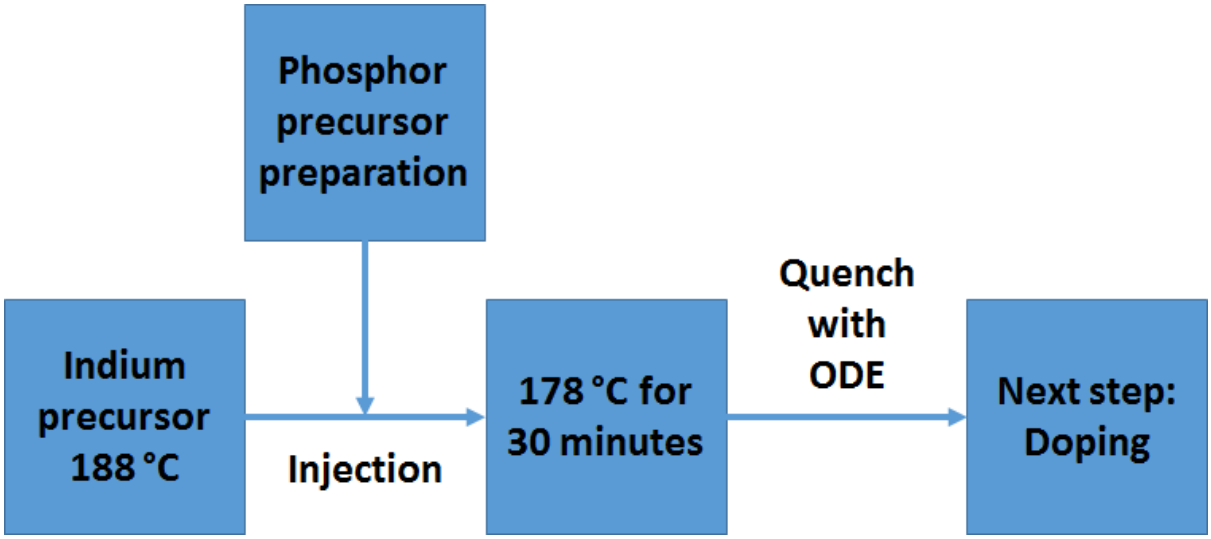

Figure 30: Schematic overview of the protecol to synthesize InP QDs. First, the indium precursor was heated to 188°C, before it was injected with the phosphor precursor. After 30 minutes of reacting, the reaction was quenched with ODE.

Post-synthesis doping method

In preparation of copper doping, a solution of *X* M $Cu(st)_2$ in ODE was prepared (1.25 ml was needed for the doping of ¼ of the previous reaction mixture). This solution was heated to 130 °C until the $Cu(st)_2$ was fully dissolved in ODE.

The raw reaction mixture from the core synthesis was heated to 130 °C. Upon reaching this temperature, the prepared $Cu(st)_2$ solution was added dropwise to the reaction mixture. The hotplate was set at 145–150 °C and every 5 minutes the hotplate temperature is increased with 5-7 °C, adjusting

the hotplate temperature in such a manner that the temperature rate of the mixture was equal to 1 °C/minute. Upon reaching 220 °C, the reaction mixture was cooled down by removing the hotplate. After the reaction, the reaction mixture was used for shell growth.

Shell growth upon InP cores using SILAR

Before SILAR, precursors were prepared, starting with the zinc precursor. A 0.1 M $Zn(st)_2$ solution in ODE was prepared in around bottom flask on a slenck line. First the mixture of $Zn(st)_2$ and ODE was flushed with nitrogen, three times, followed by heating the mixture to ~130 °C, until the $Zn(st)_2$ was dissolved. Next, the solution was degassed at 100 °C under vacuum for a couple of hours, before it was moved into the glovebox. The 0.1 M solutions of Se and S in TOP were prepared in the glovebox with degassed ODE.

Shell growth was performed according to three main steps (upper scheme of Figure 31). First, the raw reaction mixture was heated to 150 °C, followed by the shell growth cycles. Lastly, the reaction mixture was cooled down to room temperature. The shell growth cycles are depicted in the lower scheme of Figure 31. Cationic precursor ($Zn(st)_2$ in ODE at 130 °C) was dropwise added to the raw reaction mixture, followed by 10 minutes of vigorous stirring. Next, the anionic precursor (130 °C) was added to the mixture and the temperature was increased to 220 °C for 30 minutes. After 30 minutes at 220 °C, the reaction mixture was cooled to 150 °C. This was followed by the next cycle until all cycles were performed. Lastly, the reaction mixture was cooled down.

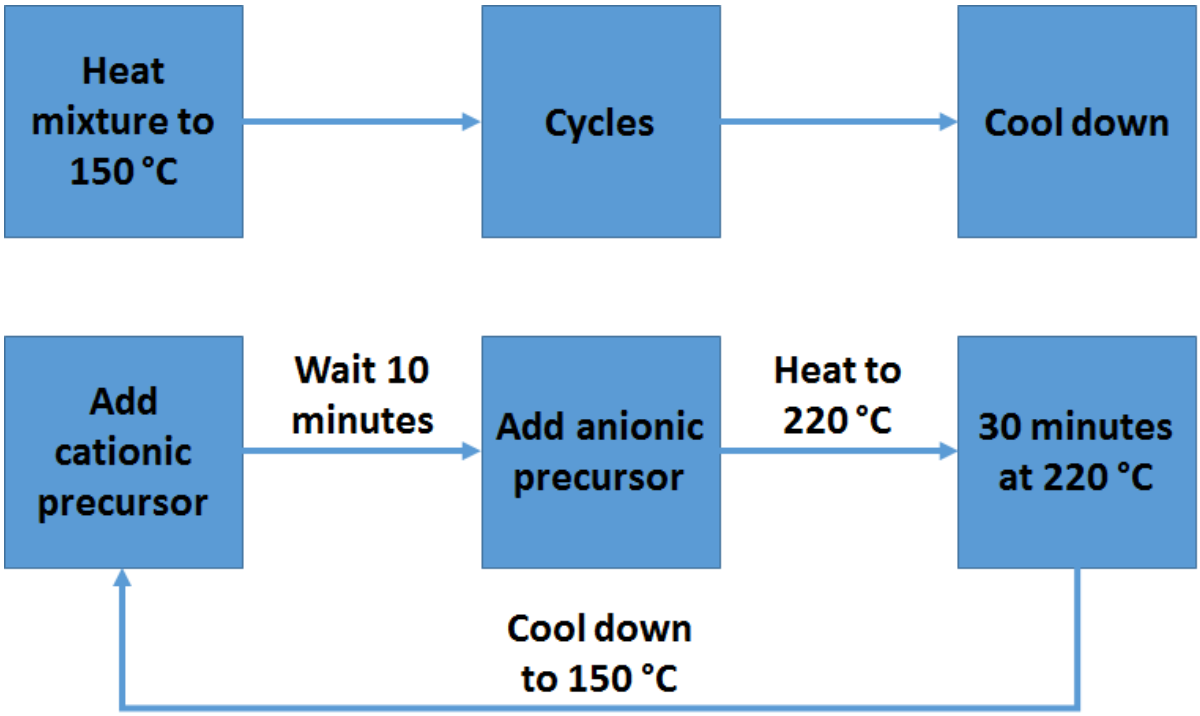

Figure 31: This scheme shows the schematic overview of the SILAR reaction. The top part is the overview of the entire reaction, while the bottom part shows a single cycle.

Appendix 3: Emission and QY measurements

Emission measurements where performed on both InP and Cu^+:InP QDs with shells of various thickness. The emission spectra for InP and Cu^+:InP are shown in Figure 32 and Figure 33 respectively. QY measurements were performed on the Cu^+:InP with 5 and 7 shells and the results are shown in Figure 34. Also QY is measured for Cu^+:InP QDs with 3 monolayers of $ZnSe_{1-x}S_x$ shell with low copper doping levels.

Emission spectra of InP QDs with various shell thicknesses

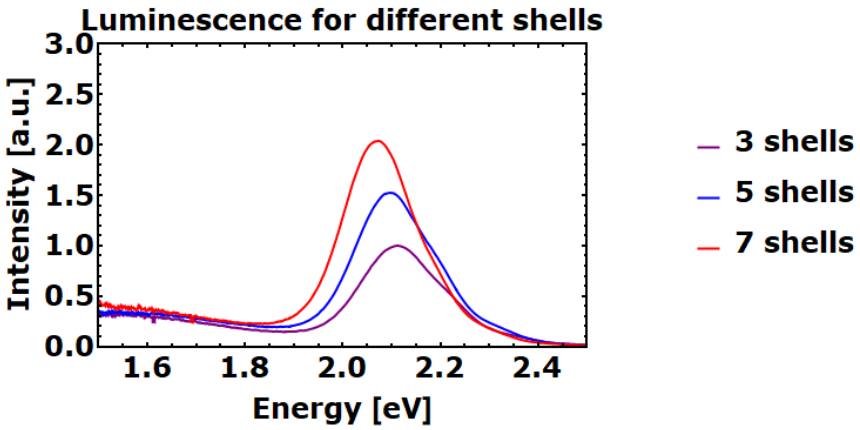

Figure 32: This graph shows the emission spectra of undoped InP QDs with different shell thicknesses. The purple, blue, and red lines represent undoped InP QDs with 3, 5, and 7 monolayers of shell, respectively. The S transition peak position is around 2.1 eV. The photoluminesence of the QDs increases upon the growth of thicker shells, which is because the excitons get confined to the core and the probability of tunneling to a surface trap state decreases upon growing a thicker shell. A redshift in peak position is observed upon shell growth as well. The broad emission band at energies lower than 1.9 eV is trap emission and does not seem to change upon growing shells thicker than 3 monolayers. Meaning that this trap emission is likely from defects within the crystal structure of the cores or from surface trapes of the InP cores which are not passivated due to lattice mismatches and defects within the first monolayers of the shell. The emission spectra are corrected for the absorption at the excitation wavelength (395 nm) and are normalized for the 3 monolayer shell sample.

Emission spectra of Cu^+:InP QDs with various shell thicknesses

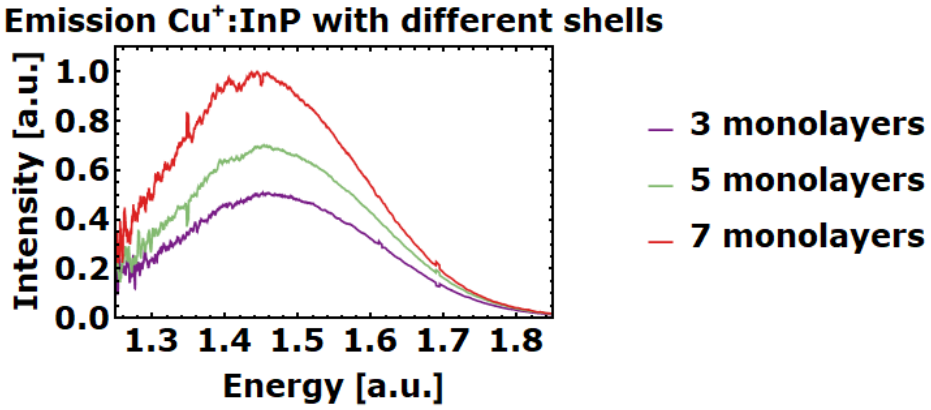

Figure 33: This graph shows the emission spectra of Cu^+:InP QDs with different shell thicknesses. The purple, green, and red lines represent Cu^+:InP QDs with 3, 5, and 7 monolayers of shell, respectively. Similarly to the undoped InP QDs, the photoluminesence of the QDs increases upon the growth of thicker shells, however the peak position is down-shifted from

~2.1 eV for the undoped to~ 1.45 eV for the Cu⁺:InP QDs, due to the L_{CB}MCT emission mechanism. The emission spectra are corrected for the absorption at the excitation wavelength (395 nm) and are normalized for the 3 monolayer shell sample.

QY measurements of Cu⁺:InP QDs with 5 and 7 monolayers of shell

Sample information:
$Cu(st)_2$ added in doping phase: 1.25 ml 0.008M in ODE
Shell thickness: 5 and 7 monolayers

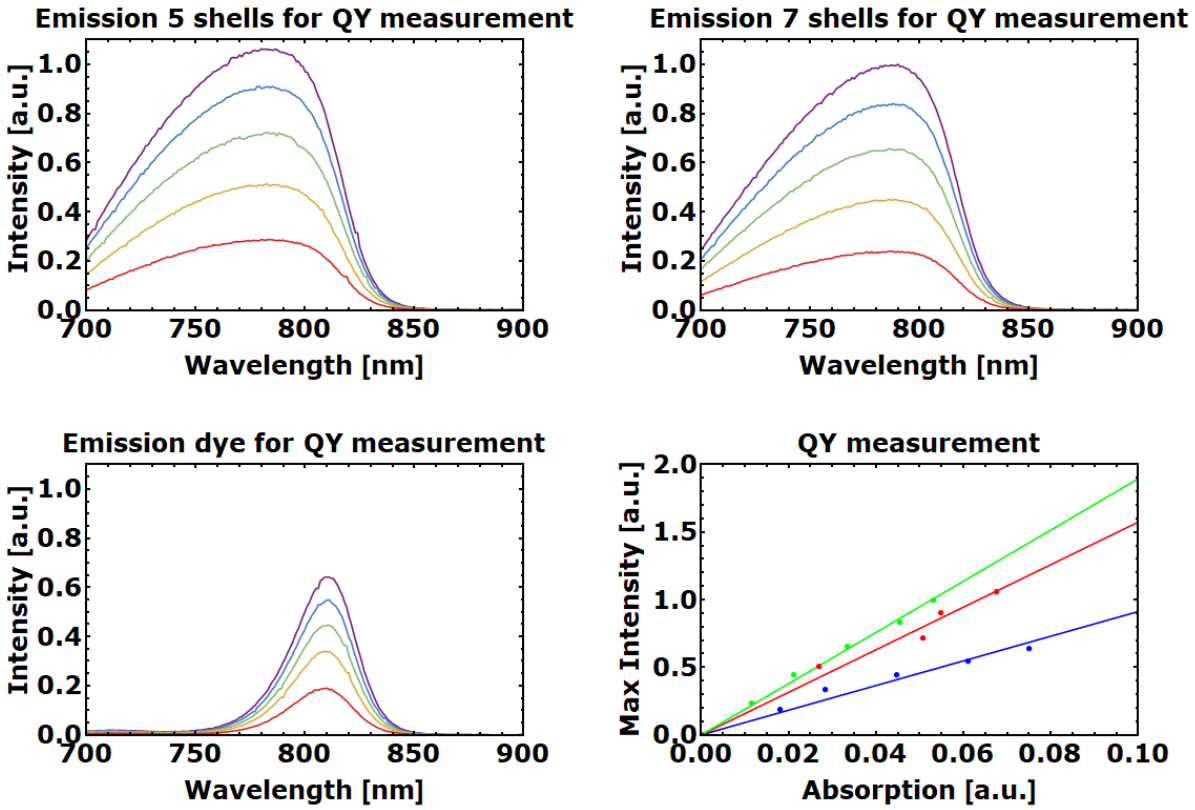

Figure 34: The graphs on the top-left, top-right, and bottom-left show emission spectra of dilution series of Cu⁺:InP QDs with 5 shells, 7 shells, and a dye (QY of 12%), respectively. Bottom-right) This graph shows the maximum emission for each dilution of each sample and the dye as function of the absorption at 678 nm (excitation wavelength).The blue, red, and green lines are the dye, 5 monolayer sample and 7 monolayer sample, respectively. The slope of each line (9.12, 15.74, and 18.95 respectively) is used calculate the QY of the samples utilizing equation 27, where $\emptyset_{QD}$ and $\emptyset_{Dye}$ are the QY of the sample and dye respecitivly, $Grad_{QD}$ and $Grad_{Dye}$ are the slopes, and ${n_{QD}}^2$ and ${n_{Dye}}^2$ are refractive index of the solvents of the sample and dye. The QY of the 5 and 7 monolayer samples are 21 and 26% respectively.

$$\emptyset_{QD} = \emptyset_{Dye} \frac{Grad_{QD}}{Grad_{Dye}} * \frac{{n_{QD}}^2}{{n_{Dye}}^2} \quad (27)$$

QY measurements of Cu^+:InP 3 monolayers of shell and low copper dopant concentration

Sample information:
$Cu(st)_2$ added in doping phase: 1.25 ml 0.001M in ODE
Shell thickness: 3 monolayers

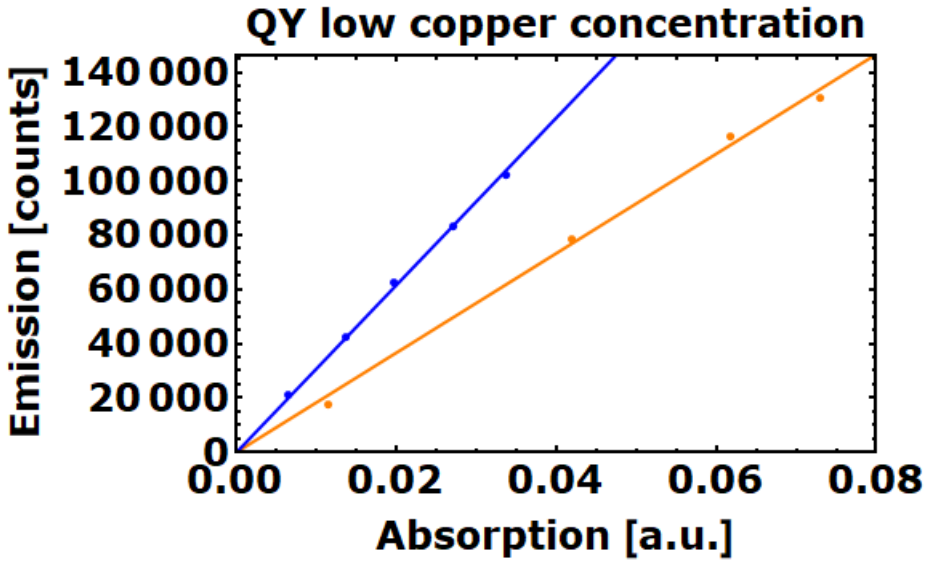

Figure 35: The QY is determined in the same way as above. The graph shows the maximum luminescence of dilution series of a dye (orange) and the sample (blue) as function of the absorption at the excitation wavelength (678 nm). The slopes are used in combination with equation 27 inorder to calculate the QY. The calculated QY was 21%.